Tuning electronic and morphological properties for high-performance wavelength-selective organic near-infrared cavity photodetectors

Jochen Vanderspikken, Quan Liu*, Zhen Liu, Tom Vandermeeren, Tom Cardeynaels, Sam Gielen, Bruno Van Mele, Niko Van den Brande, Benoît Champagne, Koen Vandewal*, Wouter Maes*

J. Vanderspikken, Dr. Q. Liu, T. Vandermeeren, Dr. T. Cardeynaels, Dr. S. Gielen, Prof. K. Vandewal, Prof. W. Maes
Hasselt University, Institute for Materials Research (IMO), Agoralaan, 3590 Diepenbeek, Belgium
IMEC, Associated Lab IMOMEC, Wetenschapspark 1, 3590 Diepenbeek, Belgium

Z. Liu, Prof. B. Van Mele, Prof. N. Van den Brande
Vrije Universiteit Brussel, Physical Chemistry and Polymer Science, Pleinlaan 2, 1050 Brussels, Belgium

Dr. T. Cardeynaels, Prof. B. Champagne
University of Namur, Laboratory of Theoretical Chemistry, Theoretical and Structural Physical Chemistry Unit, Namur Institute of Structured Matter, Rue de Bruxelles 61, 5000 Namur, Belgium

E-mail: quan.liu@uhasselt.be, koen.vandewal@uhasselt.be, wouter.maes@uhasselt.be

Incorporation of compact spectroscopic near-infrared (NIR) light detectors into various wearable and handheld devices opens up new applications, such as on-the-spot medical diagnostics. To extend beyond the detection window of silicon, i.e. past 1000 nm, organic semiconductors are highly attractive because of their tunable absorption. In particular, organic NIR wavelength-selective detectors have been realized by incorporating donor:acceptor thin films, exhibiting weak intermolecular charge-transfer (CT) absorption, into an optical microcavity architecture. In this work, the alkyl side chains of the well-known PBTTT donor polymer are replaced by alkoxy substituents, hereby red-shifting the CT absorption of the polymer:$PC_{61}BM$ blend. We show that the unique fullerene intercalation features of the PBTTT polymer are retained when half of the side chains are altered, hereby maximizing the polymer:fullerene interfacial area and thus the CT absorption strength. This is exploited to extend the detection range of organic narrow-band photodetectors with a full-width-at-half-

maximum of 30–38 nm to wavelengths between 840 and 1340 nm, yielding detectivities in the range of 5×10^{11} to 1.75×10^{10} Jones, despite the low CT state energy of 0.98 eV. The broad wavelength tuning range achieved using a single polymer:fullerene blend renders this system an ideal candidate for miniature NIR spectrophotometers.

1. Introduction

Near-infrared (NIR) light detection using organic photodetectors (OPDs) allows to miniaturize surveillance, imaging, and spectroscopic devices, e.g. for medical applications such as functional brain imaging and the detection of viral diseases.[1–3] Organic semiconductor devices are potentially cheap, flexible, and light-weight due to their mild and easily scalable processing conditions on various substrates[4,5] and they can be directly integrated on complementary metal oxide semiconductor (CMOS) readout circuitry.[6,7] This allows for a facile miniaturization and implementation of this technology into handheld devices.[8] Broad-band photodetectors commonly utilize (ultra)low bandgap materials to detect lower energy NIR light.[9,10] However, the decreasing energy gap results in high dark currents and compromised detectivities.[11] For applications requiring narrow-band detection, several strategies have been proposed, including the use of narrow-band absorbers,[12] charge collection narrowing,[13] and resonant microcavity device architectures[14]. The latter is especially promising since such devices are electronically thin, yet optically thick at the resonance wavelength,[15,16] which is simply determined by the total thickness of the photoactive film and the transport layers sandwiched between the (semi)reflecting electrodes constituting the microcavity.[14]

Optical cavity devices have shown a broad wavelength tunability and applicability beyond 1000 nm by using the weak but broad charge-transfer (CT) absorption originating from intermolecular optical transitions at the interface of electron donor and acceptor type organic materials.[17] These transitions at photon energies below the optical gap of both the donor and acceptor have been extensively studied and have been linked to the open-circuit voltage in

2

organic photovoltaics[18,19] as well as the minimum achievable dark current in OPDs.[11] In order to efficiently extend the detection window toward lower energy infrared light, two fundamental material design criteria need to be addressed. First, the intermolecular energy gap or CT state energy, approximated by the difference between the highest occupied molecular orbital (HOMO) of the donor and lowest unoccupied molecular orbital (LUMO) of the acceptor molecules, must be decreased to make lower energy sub-bandgap transitions available.[17,20] Secondly, the CT transitions must occur sufficiently frequent to achieve a threshold absorption coefficient for which cavity enhancement enables a reasonably high external quantum efficiency (EQE) at the resonance wavelength.[14] Since direct CT absorption is an intermolecular and thus inherently weak process, maximizing the amount of interface between the donor and acceptor is crucial. The most successful material system fulfilling these criteria to date is the intercalating system comprising poly[2,5-bis(3-tetradecylthiophen-2-yl)thieno[3,2-b]thiophene] (PBTTT) and [6,6]-phenyl-C_{61}-butyric acid methyl ester ($PC_{61}BM$),[21] which has shown its employability for cavity-enhanced NIR photodetection until 1000 nm. Extending the detection range to longer wavelengths was hampered due to the sharply decreasing CT absorption efficiency around 1.2 eV.[14]

The occurrence of conjugated polymers which, similarly to PBTTT, allow intercalation of fullerene acceptors and other small molecules into their crystal structure is rather limited and highly dependent on the structural properties of the donor polymer.[22] So far, no structural alterations for solution-processable materials have been shown to decrease the CT state energy while maintaining a relatively high CT absorption strength at longer wavelengths. In this work, it is demonstrated that a novel side chain-engineered PBTTT-OR-R (alkoxy-alkyl) polymer is able to fulfil both the electronic and morphological blend requirements to extend the direct CT absorption to longer wavelengths. Additionally, it is shown that another side chain variant, the fully alkoxylated PBTTT-$(OR)_2$, does not yield the desired blend requirements. Using rapid heat-cool calorimetry (RHC) and X-ray diffraction (XRD) techniques, we find that the polymer

for which half of the alkyl side chains are replaced by alkoxy counterparts maintains its (semi)crystalline and intercalating behavior. Fourier-transform photocurrent spectroscopy (FTPS) shows red-shifted, yet relatively strong CT absorption. When applied into a microcavity OPD, the PBTTT-OR-R:$PC_{61}BM$ devices are among the best-performing wavelength-tunable NIR OPDs with detectivities in the 1000–1340 nm wavelength range.

2. Results and discussion

The intercalating nature of the PBTTT:$PC_{61}BM$ blend provides a large interfacial area between the donor and acceptor molecules and therefore rather efficient direct CT absorption. The synthetic challenge is therefore to design a polymer with a high HOMO level which still allows $PC_{61}BM$ intercalation, hereby keeping the CT absorption coefficient rather high while pushing it further into the NIR. We hypothesized that (partial) substitution of the alkyl side chains of PBTTT for stronger electron-donating alkoxy side chains could allow to achieve this.[23] To estimate the influence of the replacement of alkyl by alkoxy side chains on the bithiophene moiety of PBTTT on the frontier orbital energy levels (in particular the HOMO), density functional theory (DFT) calculations (M06/6-311G(d)) were carried out (see Supporting Information (SI) for details; Table S1). The HOMO level of the pristine PBTTT ($HOMO_{calc}$: – 4.95 eV) is predicted to significantly increase (by 0.37 eV) upon introduction of the oxygen atoms in the side chains ($HOMO_{calc}$ PBTTT-$(OR)_2$: –4.58 eV). The hybrid version, in which the bithiophene carries both an alkyl and an alkoxy side chain, has an intermediate value ($HOMO_{calc}$ PBTTT-OR-R: –4.88 eV).

These rationally designed polymers were subsequently synthesized. An overview of the synthesis pathways toward PBTTT and its novel variants is depicted in **Scheme 1**. Details of the synthesis of the thiophene precursors, 2-bromo-3-tetradecylthiophene (Th-R) and 2-bromo-3-(tetradecyloxy)thiophene (Th-OR), can be found in the SI. A palladium-catalyzed direct C-H coupling of Th-R and Th-OR yielded three bithiophene building blocks with increasing electron

4

density.[24–26] Next to obtaining the previously reported alkyl (BiT-R$_2$) and alkoxy-substituted bithiophene (BiT-(OR)$_2$), the novel asymmetric alkyl-alkoxy-bithiophene (BiT-OR-R) was also obtained from a single reaction. Because of the significant increase in polarity that the oxygen atom brings to the bithiophene structure, the resulting mixture of three products was separated with relative ease using silica column chromatography. The polymers were subsequently prepared through palladium-catalyzed Stille cross-coupling polymerization (Scheme 1). The PBTTT polymer was made in a microwave reactor under similar conditions as originally reported by McCulloch *et al.*[27] For the polymerizations toward PBTTT-OR-R and PBTTT-(OR)$_2$, the catalytic system was changed to tetrakis(triphenylphosphine)palladium(0) and the polymerization was carried out using conventional heating. An overview of the obtained molar mass characteristics for the three polymers can be found in Table S2 (with the chromatograms in Figure S1).
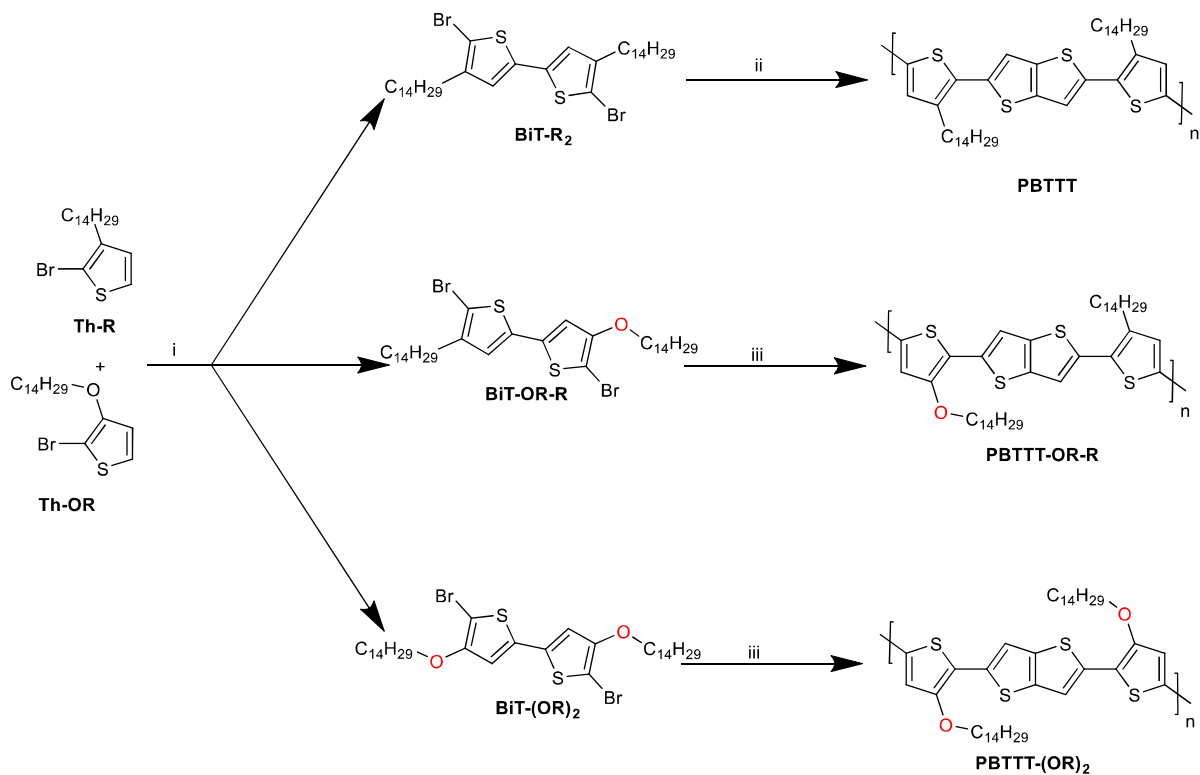
Scheme 1: (a) Synthesis pathway toward PBTTT, PBTTT-OR-R, and PBTTT-(OR)$_2$: (i) AgNO$_3$, KF, Pd(PhCN)$_2$Cl$_2$, DMSO; (ii) 2,5-bis(trimethylstannyl)thieno[3,2-*b*]thiophene, Pd$_2$(dba)$_3$, P(*o*-tol)$_3$, chlorobenzene, μwave; (iii) 2,5-bis(trimethylstannyl)thieno[3,2-*b*]thiophene, Pd(PPh$_3$)$_4$, toluene/DMF.

Thermogravimetric analysis (TGA) was carried out to judge the thermal stability of the polymers and to determine the upper temperature limit for thermal analysis by RHC (vide infra). All polymers showed an onset of degradation above 300 °C (Table S2). The three polymers were subsequently analyzed by UV-Vis-NIR absorption spectroscopy and cyclic voltammetry (CV) to get an estimate of the energy level shifts upon introduction of the alkoxy side chains. The introduction of alkoxy side chains shifts the wavelength (λ_{max}) at which the polymers have their maximum absorption in film. PBTTT has its maximum at 529 nm, while PBTTT-OR-R and PBTTT-(OR)$_2$ show a λ_{max} at 580 nm and 603 nm, respectively (Table S2, Figure S2). Absorption onsets are situated at 638, 675, and 715 nm for PBTTT, PBTTT-OR-R and PBTTT-(OR)$_2$, respectively. The replacement of alkyl by alkoxy side chains does not strongly affect the LUMO energy level and almost exclusively influences the HOMO of the polymers (Table S2, Figure S3–S4). Introduction of one alkoxy side chain results in a HOMO level increase of 0.25 eV (from −5.12 to −4.87 eV), while insertion of two alkoxy substituents shifts the HOMO upward by 0.42 eV (to −4.70 eV) as compared to PBTTT. While the absolute values of the estimated experimental HOMO levels differ from the calculated ones, the trend upon replacing alkyl by alkoxy side chains agrees reasonably well with the DFT calculations.

To determine the effect of side chain substitution on the optical CT transitions, bulk heterojunction (BHJ) blends of the polymers with PC$_{61}$BM were analysed in an inverted photodiode stack ITO/ZnO/polymer:PC$_{61}$BM/MoO$_3$/Ag, which has a minimum of interference effects for thin photoactive layers (sample preparation details in SI). In order to characterize the CT absorption band, the external quantum efficiency (EQE) spectra were measured with high sensitivity using Fourier-transform photocurrent spectrosopy (FTPS)[19] (**Figure 1**). The lower energy transitions are significantly more red-shifted when using PBTTT-OR-R as compared to PBTTT as a consequence of the increased polymer HOMO level. The highest HOMO material, PBTTT-(OR)$_2$, has an even more extended CT absorption band. However, the overall EQE is

about 3 times lower. Only at wavelengths longer than 1400 nm, PBTTT-(OR)$_2$ has a higher EQE than PBTTT-OR-R, but the EQE values remain very low (< 0.05%) due to the very weak CT absorption in that spectral region.
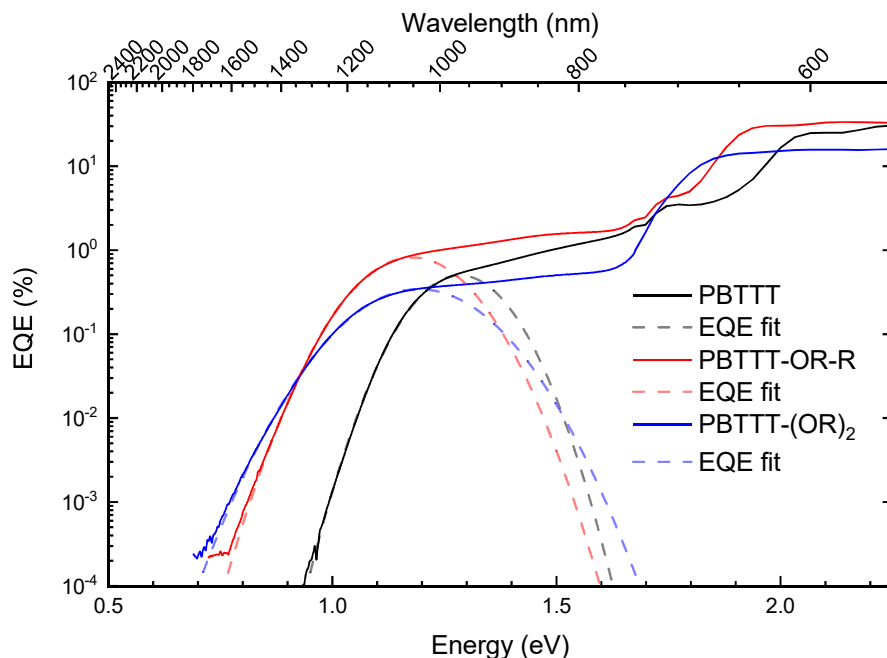

Figure 1: EQE spectra for PBTTT (black), PBTTT-OR-R (red), and PBTTT-(OR)$_2$ (blue) blends with PC$_{61}$BM in an inverted ITO device stack (glass/ITO/ZnO/active layer/MoO$_3$/Ag): EQE vs wavelength shows a significant extension of CT absorption to longer wavelengths due to the introduction of alkoxy side chains. EQE vs energy and the fitted curves (dashed black, red, and blue lines), illustrating decreasing E_{CT} gaps of 1.15, 0.98, and 0.89 eV for PBTTT, PBTTT-OR-R, and PBTTT-(OR)$_2$, respectively (see SI for fitting details).

The energy of the CT state onset, E_{CT}, was determined by fitting the CT absorption band onset with a Gaussian function derived from Marcus theory (Figure 1 and Table S2; fitting details in the SI).[28,29] E_{CT} significantly lowers from 1.15 eV for PBTTT:PC$_{61}$BM to 0.98 eV for the PBTTT-OR-R:PC$_{61}$BM system, i.e. a red-shift of 0.17 eV, which is a bit less than the change in HOMO energy level estimated by CV (0.25 eV). Replacement of all alkyl by alkoxy side chains in PBTTT-(OR)$_2$ shifts E_{CT} by another 0.26 eV, affording 0.89 eV. Also this shift is lower than the estimated shift in HOMO energy levels (0.42 eV) determined by CV. This observation underlines once more that, while changes in frontier orbital energy levels will qualitativily agree with changes in CT state energies, it is hard to be quantitatively predictive.

One should not forget that the frontier orbital energy levels are determined on the neat materials. As such, the electrostatic landscape at the interface and the CT state binding energy are not taken into account. Additionally, the CT absorption of the blend is broad and almost constant in the energy range 1.1–1.6 eV, which is rather unique. This is likely the result of a superposition of several possible types of CT transitions to higher energy electronic or vibrational states, each with a Gaussian(-like) line shape. As blend performance and detectivity parameters strongly depend on the morphology of the photoactive layer, the pristine polymers, $PC_{61}BM$, and their 1:1 mixtures (i.e. approximately the stoichiometric composition of the co-crystal) were analyzed by RHC as a probe for crystallinity (**Figure 2**). The pristine polymers all show side chain melting below 70 °C, followed by a liquid crystal transition in the case of PBTTT.[30] At elevated temperatures, all polymers exhibit a backbone melting (which is indicated in Figure 2 for PBTTT and PBTTT-OR-R by arrows). In the case of PBTTT-$(OR)_2$, a spread-out melting transition can be observed, which extends beyond the onset of degradation as determined by TGA, and was therefore not studied further. RHC measurements performed on the 1:1 mixtures indicate that a new melting peak is formed for PBTTT when mixed with $PC_{61}BM$ at approximately 230 °C, which is completely absent in the thermograms of the pristine components and has previously been attributed to melting of the co-crystal of PBTTT and $PC_{61}BM$.[22,31] A similar, albeit smaller new melting peak can be observed at ~220 °C for the novel PBTTT-OR-R variant mixed with $PC_{61}BM$, which is again not present in the pristine components. For the PBTTT-$(OR)_2$ material, on the other hand, no new melting peak is observed when blended with $PC_{61}BM$. The RHC thermograms of the 1:4 mixtures (Figure S9), as used for device preparation, show similar behaviour as observed for the 1:1 mixtures, i.e. the appearance of a new melting peak at the same temperature as in the 1:1 mixtures for PBTTT and the novel PBTTT-OR-R variant mixed with $PC_{61}BM$, and no new melting peak for the PBTTT-$(OR)_2$:$PC_{61}BM$ mixture. In addition, a new melting peak can now be observed originating from the excess of $PC_{61}BM$, preceded by its cold crystallization. An in-depth study

of the full phase behavior of these systems falls outside the scope of the present work and will
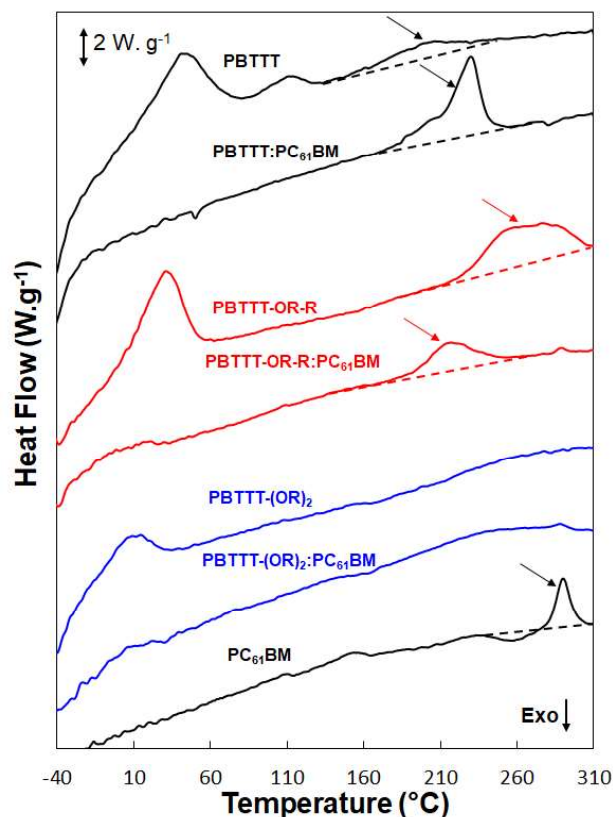
be the topic of a forthcoming publication.

Figure 2: Rapid heat-cool calorimetry measurements (2nd heating) for the PBTTT polymer series, the respective 1:1 mixtures with $PC_{61}BM$, and pure $PC_{61}BM$. Arrows indicate the backbone melting of PBTTT and PBTTT-OR-R, the melting peak of $PC_{61}BM$, and the two new melting peaks observed for the 1:1 mixtures containing PBTTT and PBTTT-OR-R. The curves were vertically shifted for clarity.

To further investigate if the melting behavior observed for the novel materials is caused by

intercalation of $PC_{61}BM$ within the polymer crystallites, XRD analysis of the polymers and

their blends was carried out (**Figure 3**). The *d*-spacing for the neat PBTTT polymer and its 1:1

mixture with $PC_{61}BM$ amounts to 21.3 and 28.9 Å, respectively. This increase in *d*-spacing is

consistent with literature[32] and has been attributed to the intercalation of $PC_{61}BM$ in between

the PBTTT side chains, pushing the backbones further apart.[21,30,32] When looking at PBTTT-

OR-R, also here the *d*-spacing increases significantly upon blending with $PC_{61}BM$, from 22.6

to 28.2 Å. For the PBTTT-(OR)$_2$ material, however, a minor increase from 23.4 to 25.3 Å is

9

observed. These results suggest that intercalaction with $PC_{61}BM$ is likely maintained for the PBTTT-OR-R material, while its presence is for sure less pronounced for the mixture containing PBTTT-$(OR)_2$. Further studies to get a deeper insight into the phase behavior of these novel blends, the optimal polymer:$PC_{61}BM$ ratio for intercalation, and the origin of the reduction (or even complete absence) of intercalation in the PBTTT-$(OR)_2$:$PC_{61}BM$ blend are ongoing. Nevertheless, current insights allow to explain why the sub-bandgap CT absorption is still significant for PBTTT-R-OR at lower energy wavelengths, as close mixing due to intercalation allows for a large interfacial area and a relatively efficient CT absorption.
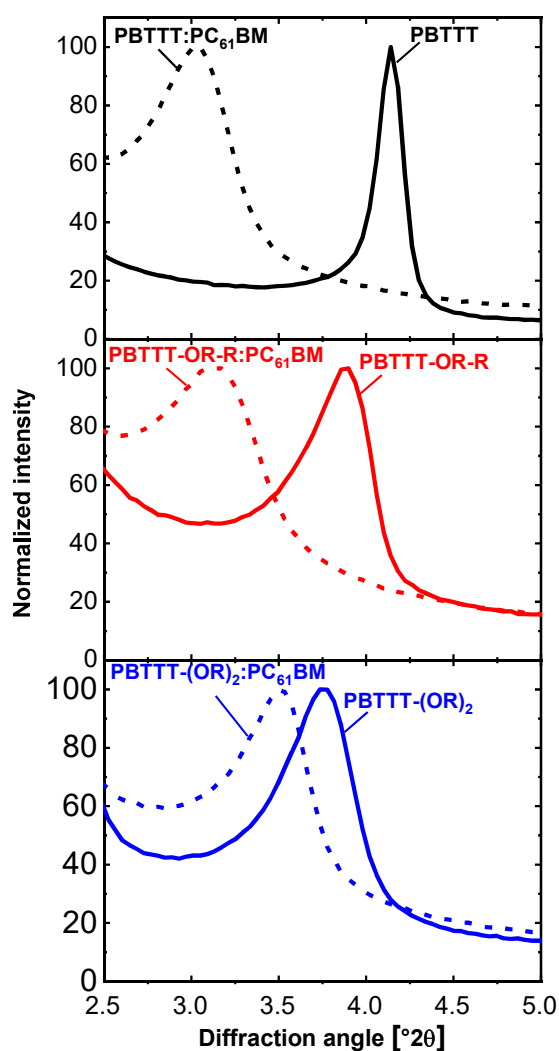
Figure 3: X-ray diffraction patterns for the pristine polymers (solid lines) and 1:1 mixtures with $PC_{61}BM$ (dashed lines).

To achieve a high-performance detector with a high specific detectivity (D^*), a low dark current density (J_D) is crucial. However, recent work has shown that for low E_{CT} devices ($E_{CT} <$ ~0.9 eV), the dark current becomes intrinsically limited by the photoactive material blend, exponentially increasing with decreasing E_{CT}.[11] **Figure 4** shows current density-voltage (J-V) curves measured in the dark for the different polymer:$PC_{61}BM$ blends in inverted ITO-based device stacks for two different active layer thicknesses (device preparation details can be found in the experimental section). For all three material systems, the J-V curves in the reverse voltage region do not depend strongly on the active layer thickness. However, a clear trend of the dark current with E_{CT} is observed. The lowest dark current is obtained for PBTTT:$PC_{61}BM$ and it increases about one order of magnitude for the PBTTT-OR-R blend and three orders of magnitude for PBTTT-$(OR)_2$:$PC_{61}BM$ (Figure 4).
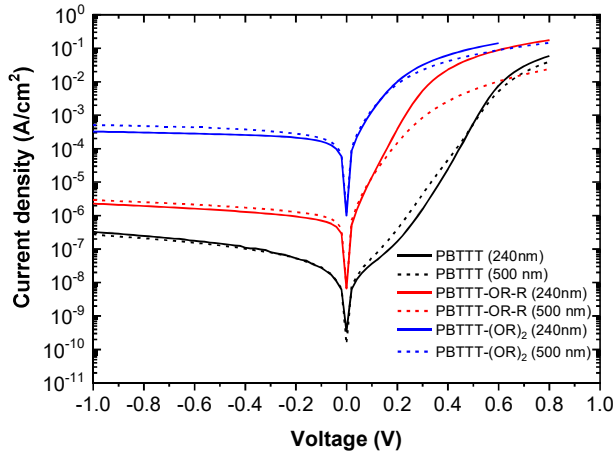
Figure 4: Dark current densities as a function of voltage obtained for PBTTT, PBTTT-OR-R, and PBTTT-$(OR)_2$ blends with $PC_{61}BM$ with a thickness of 240 and 500 nm in inverted ITO device stacks.

A lower limit for the absolute value of the dark current density at reverse voltages can be calculated based on measurements of the absolute value of the photocurrent density (J_{Ph}) and open-circuit voltage (V_{OC}) of devices under illumination (experimental details in SI).[11]

$$J_D > J_{Ph} e^{-V_{OC}\frac{q}{kT}} \tag{1}$$

For the PBTTT-OR-R and PBTTT-(OR)$_2$ devices, this corresponds to a lower limit to J_D of 5.7 $\times$ 10^{-7} A/cm^2 and 1.1 $\times$ 10^{-4} A/cm^2, respectively. The measured J_D values at -1 V, 2.3 $\times$ 10^{-6} and 3.2 $\times$ 10^{-4} A/cm^2, respectively, are within a factor of 4 from these lower limits (**Table 1**). This indicates that, for these devices, the mechanisms determining J_D are similar to those limiting their V_{OC}, known to be intrinsic to the photoactive layer and resulting in a linear dependence of V_{OC} on E_{CT}.[11] Using this correlation in Equation (1), one finds indeed that J_D exponentially depends on E_{CT}, as previously reported for donor:acceptor blends with an E_{CT} in the range of 0.9 eV (or smaller).[11] For PBTTT:PC$_{61}$BM, we obtain a measured J_D at -1 V being much larger (by 5 orders of magnitude) than the lower limit calculated via Equation (1). This can be attributed to the presence of pinholes, traps and/or injection of charge carriers from the electrode contacts, causing additional dark current on top of the ideal diode dark current.[33] The dark current for this material blend is therefore not limited by intrinsic bulk properties. The ratio $J_D/J_{D,V_{OC}}$ will approach unity when the device is intrinsically limited by bulk properties and will be much larger than 1 when extrinsic factors are present (Table 1). For PBTTT, this ratio is in the order of 10^4 while PBTTT-OR-R and PBTTT-(OR)$_2$ show a value close to 1, indicating that the latter are more bulk-limited systems.

Table 1: Overview of the obtained E_{CT}, V_{OC}, J_{Ph}, and J_D values for the PBTTT polymer series blended with PC$_{61}$BM in ITO devices and the calculated V_{OC}-limited dark current, $J_{D,V_{OC}}$, and the $J_D/J_{D,V_{OC}}$ ratio, showing the proximity for the three material blends to being intrinsically limited by bulk properties.

Material	E_{CT} [eV]	V_{OC} [V]	J_{Ph} [A/cm^2]	J_D (at -1 V) [A/cm^2]	$J_{D,V_{OC}}$ [A/cm^2]	$J_D/J_{D,V_{OC}}$
PBTTT	1.15	0.53	4.5 $\times$ 10^{-3}	3.0 $\times$ 10^{-7}	5.0 $\times$ 10^{-12}	6.0 $\times$ 10^4
PBTTT-OR-R	0.98	0.23	4.4 $\times$ 10^{-3}	2.3 $\times$ 10^{-6}	5.7 $\times$ 10^{-7}	4.0
PBTTT-(OR)$_2$	0.89	0.09	3.5 $\times$ 10^{-3}	3.2 $\times$ 10^{-4}	1.1 $\times$ 10^{-4}	2.9

As the CT absorption is significantly extended to longer wavelengths for PBTTT-OR-R:PC$_{61}$BM as compared to PBTTT:PC$_{61}$BM, while retaining similar EQE values in the CT band (Figure 1), this blend was used in an optical cavity device. PBTTT-(OR)$_2$:PC$_{61}$BM, on the other

hand, was not further pursued due to the high (intrinsically limited) dark current and low EQE for this combination. The resonance wavelength of the Fabry-Pérot cavity is proportional to the effective refractive index of the photoactive layer and the thickness of the cavity.[34] Based on optical transfer matrix model simulations, the required blend thicknesses were estimated to achieve narrow-band resonances between 842 and 1340 nm (Figure S10).[35] The optimized device stack consists of the active layer with ZnO as electron transport layer and MoO_3 as hole transport layer sandwiched between a non-transparant (thick) and a semi-transparant (thin) Ag electrode on a glass substrate (see **Figure 5a**). Measured dark currents of the cavity devices are comparable to the dark currents observed in the optimized ITO devices (Figure S11). EQEs from 18.3% at 842 nm and 0.6% at 1340 nm were achieved with narrow peak responses with a full-width-at-half-maximum (FWHM) between 30 and 38 nm (Figure 5b and 5d, respectively). The cavity-based detectors still show a significant response below 800 nm (Figure S12), which can be supressed using a thin layer of PBTTT, as previously reported, without significantly hampering device performance.[14] Atomic force microscopy (Figure S13) showed no clear signs of phase separation and a very low surface roughness for all active layers. The latter is of high importance to minimize fluctuations in the thickness of the cavity and to maintain a narrow detector response. From the current density-voltage response of these photodetectors, the shunt resistance (R_{sh}) at 0 V was extracted to be around 0.1 $M\Omega.cm^2$, rather independent of active layer thickness.[36] A lower limit to the noise current spectral density (j_{noise}, in units $A.Hz^{-1/2}.cm^{-1}$) of the photodetector, taking shot and thermal noise into account, can be calculated using the following relationship:

$$j_{noise} = \sqrt{2qJ_D + \frac{4k_bT}{R_{sh}}} \qquad (2)$$

with q the elementary charge and k_b the Boltzmann constant. When measured at short-circuit conditions, J_D will be zero and R_{sh} will determine the noise current. The calculated j_{noise} is

13

similar for all devices, around 0.3 pA.Hz$^{-1/2}$.cm^{-1}. The upper specific detectivity D^*, neglecting

other noise sources such as $1/f$ noise, is calculated using:

$$D^* = \frac{q\lambda EQE}{hc j_{\text{noise}}}$$

(3)

where h is Planck's constant and c the speed of light.[11,37] The corresponding D^* values range

between 3.2×10^{11} and 1.7×10^{10} Jones and are among the highest reported detectivities for

narrow-band OPDs (including CT absorption based cavity devices) between 1000 and 1340 nm

(Figure 5c and 6). Structural manipulation through side chain engineering of the PBTTT

polymer therefore expands the application window to longer wavelengths by significantly

redshifting the weak direct CT transition. When compared to the best detectivities achieved for

broad-band OPDs between 1120 and 1340 nm, these devices perform similarly (D^* within the

same order of magnitude) and only a simple broad band PBTTT filter is required to achieve

narrow response detectors (**Figure 6**, Table S4).
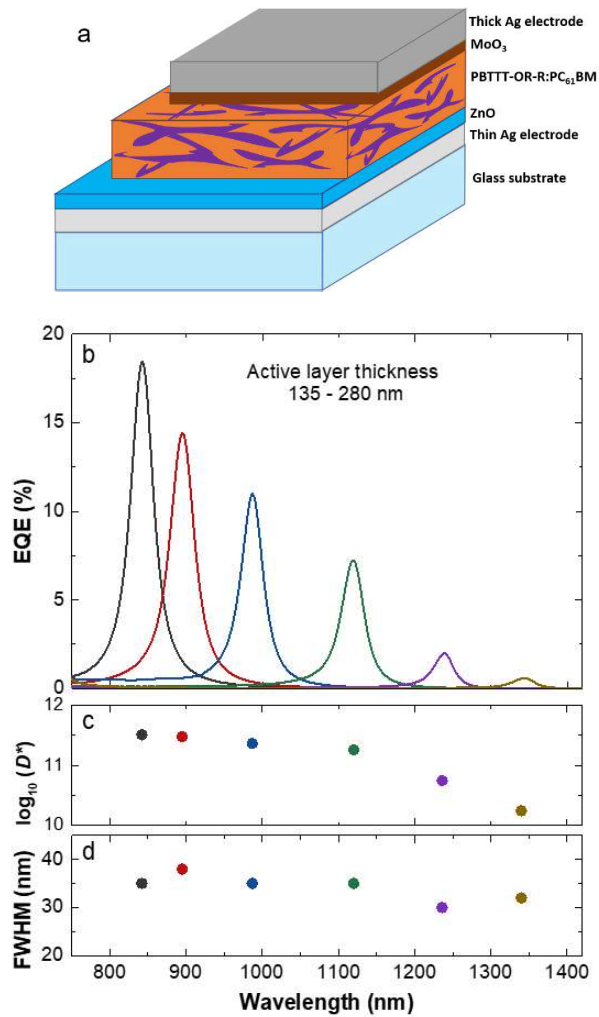
Figure 5: (a) Schematic representation of the utilized device stack for the cavity photodetectors. (b) EQEs of the metal-metal cavity device based on PBTTT-OR-R:$PC_{61}BM$ (1:4), with active layer thicknesses ranging from 135 to 280 nm. (c) Obtained detectivities between 842 and 1340 nm. (d) FWHM values of the resonance peaks.
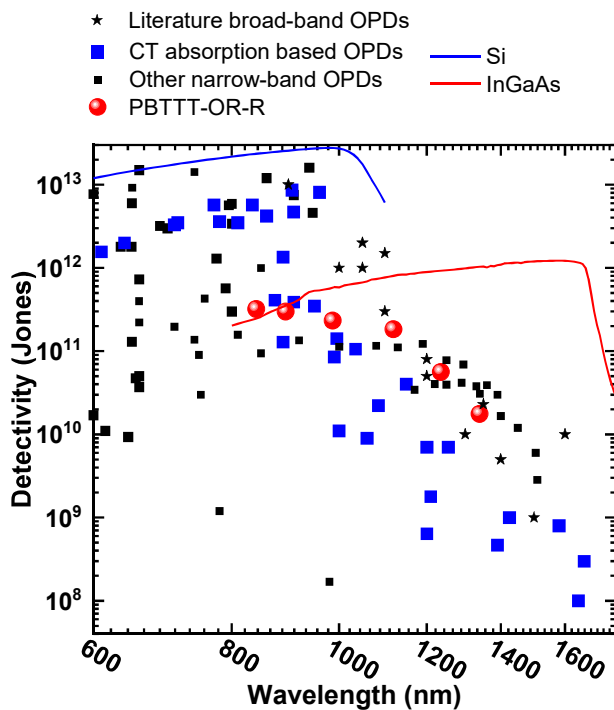
Figure 6: Comparison of the achieved performance for the PBTTT-OR-R cavity devices (red circles) to other CT absorption based cavity devices (blue squares), narrow-band (black squares), and broad-band photodetectors (black stars) (data in Table S4). For the broad-band photodetectors, the best detectivity value at a certain wavelength was taken and detectivities were determined based on either measured or calculated noise currents. The thin blue and red colored lines represent commercial inorganic photodetectors.[38]

3. Conclusion

We have tuned the electronic and morphological properties of polymer:PC$_{61}$BM blends through side chain manipulation in order to optimize the sub-bandgap charge-transfer transitions for application in microcavity organic near-infrared photodetectors. When partly replacing the alkyl side chains of PBTTT by alkoxy ones, the intercalating behavior of PC$_{61}$BM, the large donor:acceptor interfacial area, and the relatively strong CT absorption are maintained, as shown by RHC and XRD. At the same time, the higher HOMO energy level induced by the electron-donating side chains results in a significantly red-shifted CT absorption as well as an unavoidable increase in dark current. The latter is, however, close to its lower limit on the order of 0.6 μA.cm^{-2} for a donor:acceptor blend with an E_{CT} in the range of 0.9−1.0 eV. Incorporation

16

into a microcavity device results in narrow-band organic photodetectors with a detection range extended by several hundreds of nm as compared to reference PBTTT:PC$_{61}$BM cavity detectors, with state-of-the-art specific detectivities observed between 1000 and 1340 nm. With a performance comparable to the best broad-band organic photodetectors in this spectral region, this type of devices additionally allows for a broad wavelength tunability and thus compact spectroscopic applications with a diagnostic window beyond 1000 nm and without the need for additional filtering, hereby providing great potential to be applied in the next-generation of portable and wearable smart devices.

4. Experimental section

Materials and methods

All reagents and chemicals were obtained from commercial sources and used without further purification. 2,5-Bis(trimethylstannyl)thieno[3,2-*b*]thiophene was synthesized according to a literature procedure.[39,40] Solvents were dried by a solvent purification system (MBraun, MB-SPS-800) equipped with alumina columns. Reactions under microwave irradiation were performed in a CEM Discover microwave.

NMR chemical shifts (δ, in ppm) were determined relative to the residual CHCl$_3$ proton signal (7.26 ppm) or the ^{13}C resonance shift of CDCl$_3$ (77.16 ppm). Polymer molar mass distributions were estimated by size exclusion chromatography (SEC) at 160 °C on an Agilent 1260 Infinity II high temperature GPC system using a PL-GEL 10 µm MIXED-B column with 1,2,4-trichlorobenzene as the eluent and using polystyrene internal standards. Background corrected UV-Vis-NIR absorption spectra were recorded on a Cary 5000 UV-Vis-NIR spectrophotometer (Agilent) using a spectral band width of 2 nm. The optical gaps were estimated from the UV-Vis-NIR-absorption spectra of the polymer films by introducing the wavelength at the intersection of the tangent line to the low energy side of the spectrum and the x-axis in the equation E_{gap} (eV) = 1240/wavelength (nm). Cyclic voltammetry (CV) was carried out in argon-

purged acetonitrile at room temperature with an Autolab potentiostat (PGSTAT30 from Metrohm) controlled with GPES software (version 4.9) for data collection and data analysis. Tetrabutylammonium hexafluorophosphate (TBAPF$_6$) (0.1 M) was used as the supporting electrolyte. A one compartment microcell designed for three-electrode configuration was fitted with a platinum wire working electrode, a platinum wire counter electrode and an Ag/AgNO$_3$ reference electrode (Ag wire immersed in electrolyte containing 0.01 M AgNO$_3$). A film of the polymer analyte was formed on the working electrode by casting it from a chloroform solution. Voltammograms were recorded with a scan rate of 100 mV.s^{-1} under a constant flow of argon, allowing degassing and blanketing of the electrolyte before and during analysis. Typically, 5 scans per film were recorded and HOMO/LUMO energy levels were estimated from the onset potentials of the third, fourth and fifth scan. The onset potential was determined from the intersection of two tangents drawn at the rising and background current of the cyclic voltammogram. Ferrocene was used as an external standard. For calculation of the HOMO-LUMO energy levels the onset potential of oxidation/reduction, which is defined as the intersection of the linear extrapolation of the onset slope of the respective peak and the baseline, was used. For the conversion of potentials (V) obtained from the electrochemical measurements to molecular orbital energies (eV) we scale the formal potential of the Fc/Fc$^+$ redox couple to the vacuum level with a value of -4.98 eV considering that 0.0 V on the Ferrocene scale corresponds to 0.31 V versus SCE (0.55 V versus SHE) and that 0.0 V versus SHE is equivalent to -4.44 eV.[41,42] The reported HOMO/LUMO values are averaged over scans 3, 4 and 5 of multiple experiments.

HOMO/LUMO (eV) = −4.98 (eV) − E_{onset}(analyte) vs Ag/AgNO$_3$ (V) + E_f (Fc/Fc$^+$) vs Ag/AgNO$_3$ (V)

The accuracy of measuring redox potentials by CV is about 0.01−0.02 V. Reproducibility can be less because the potentials do depend on concentration and temperature.

Thermogravimetric analysis (TGA) was performed on a TA instruments TGA Q5000. Measurements were performed at a heating rate of 20 K.min^{-1} using nitrogen (25 ml.min^{-1}) as the purge gas. Sample masses of approximately 1 mg were used. The rapid heat-cool calorimeter (RHC) used for this work is a prototype instrument developed by TA Instruments that allows a relatively wide range of heating and cooling rates up to 2000 K.min^{-1}. Experiments were performed at a scanning rate of 500 K.min^{-1} with nitrogen (6 mL.min^{-1}) as the purge gas. Dedicated aluminum RHC crucibles were filled with around 200–250 µg of the respective polymer sample. A first heating was used to remove the thermal history and therefore all thermograms shown are from the second heating. XRD studies were performed with a Bruker D8 Discover using Cu Kα radiation. The samples were measured in θ−2θ scan mode using a parallel beam setup. The polymers or polymer:PC$_{61}$BM mixtures (6 mg/mL) were drop-casted from a solution in chlorobenzene at 80 °C onto a silicon substrate.

Device preparation and characterization

The sol-gel ZnO precursor (0.45 M) was prepared by dissolving zinc acetate dihydrate (Aldrich, 99.9%; 0.5 g) and ethanolamine (Aldrich, 99.5%; 0.14 g) in 2-methoxyethanol (Acros Organics, 99.8%; 5 mL). This solution was vigorously stirred at 60 °C for 2 h and then stirring was continued at room temperature overnight in air to complete the hydrolysis reaction. Solutions of polymer:PC$_{61}$BM (Solenne) at a total concentration of 25 or 50 mg/mL (donor:acceptor = 1:4 wt/wt in all the blends) were prepared in chloroform/*o*-dichlorobenzene (1.5/1, v/v) and stirred at 70 °C for 5 h in a N$_2$-filled glovebox before use. Standard ITO devices were fabricated using the inverted device structure glass/ITO/ZnO/active layer/MoO$_3$/Ag, whereas the cavity-OPDs were fabricated using the inverted device structure Eagle XG glass/Au (1.5 nm)/Ag (28 nm)/ZnO/active layer/MoO$_3$/Ag. For the interlayer study (Figure S6), ZnO was substituted for PEIE [poly(ethylenimine), 80% ethoxylated, 37 wt% in H$_2$O; Sigma Aldrich], which was deposited by spin-coating with a layer thickness of ~5 nm and then annealed at 100 °C for 10 min. Semitransparent thin Ag films were first fabricated by thermal evaporation ($<5 \times 10^{-6}$

mbar) with an extremely thin Au seed layer beneath.[43] The deposition rate for Au and Ag was 0.5 Å.s^{-1} and 4 Å.s^{-1}, respectively. Then, the ZnO precursor solution was spin-coated on the thin Ag electrodes at 4000 rpm and it was annealed at 150 °C in air for 20 min to form a 30 nm electron-transporting layer. The prepared samples were then transferred into a N$_2$-filled glovebox for spin-coating the active layer with varying thicknesses (140–500 nm) by adjusting the spin-casting rate and blend solution concentration. The blend thickness was monitored by a Bruker Veeco Dektak XT profilometer. The obtained EQE and dark currrent for the PBTTT-OR-R:PC$_{61}$BM blend, as shown in Figure 1 and 3, was only achieved after slow drying the active layer of the spin-coated PBTTT-OR-R:PC$_{61}$BM blend, which also has been shown to improve blend performance for PBTTT:PC$_{61}$BM blends, supposedly due to better blend morphology.[21] The peak EQE was also increased by almost 10%, while the dark current decreased approximately one order of magnitude (Figure S8). Finally, the MoO$_3$ (10 nm) hole-transporting layer and the Ag (100 nm) top electrode were sequentially deposited on top of the active layer through a shadow mask by thermal evaporation ($<5 \times 10^{-6}$ mbar) with an area of 0.06 cm^2. The freshly fabricated devices were measured in an inert atmosphere and light and dark J-V curves (forward scan with a step of 25 mV) were recorded using a Keithley 2400 Source Meter under AM1.5 1-sun illumination, provided by a solar simulator (Newport 91195A) with a silicon calibrated intensity equivalent to 100 mW.cm^{-2}, and under dark, respectively. The EQE$_{PV}$ spectrum for each cell was measured under chopped (135 Hz) monochromatic illumination from a Xe lamp (100 W, Newport) modulated by Cornerstone™ 130 Monochromator and an optical wheel chopper. The generated photocurrent from the solar cells was amplified with a Stanford Research System Model SR830 lock-in amplifier, and a calibrated Si photodiode with known spectral response was used as a reference. For the sensitive EQE measurements, an INVENIO R (Bruker Optics) with an external detector was employed. A low-noise current amplifier was used to amplify the photocurrent generated under illumination of the devices, with the illumination light modulated by the Fourier-transform

20

infrared (FTIR) setup. AFM experiments were performed with a JPK NanoWizard 3 AFM (JPK Instruments AG, Berlin, Germany) using AC mode in air. Silicon ACTA-50 tips from AppNano with cantilever length ~125 mm, spring constant ~40 N.m^{-1} and resonance frequency ~300 kHz were used. The scan angle, set point height, gain values and scan rate were adjusted according to the calibration of the AFM tip.

Supporting Information

Supporting Information is available from the Wiley Online Library or from the author.

Conflict of interest

The authors declare no conflict of interest.

Acknowledgements

Received: ((will be filled in by the editorial staff))
Revised: ((will be filled in by the editorial staff))
Published online: ((will be filled in by the editorial staff))

References

[1]   J. B. Balardin, G. A. Zimeo Morais, R. A. Furucho, L. Trambaiolli, P. Vanzella, C. Biazoli, J. R. Sato, *Front. Hum. Neurosci.* **2017**, *11*.

[2]   A. Sakudo, *Clin. Chim. Acta* **2016**, *455*, 181.

[3]   M. S. Nogueira, *Photodiagnosis Photodyn. Ther.* **2020**, *31*, 101892.

[4]   R. D. Jansen-van Vuuren, A. Armin, A. K. Pandey, P. L. Burn, P. Meredith, *Adv. Mater.* **2016**, *28*, 4766.

[5]   K. J. Baeg, M. Binda, D. Natali, M. Caironi, Y. Y. Noh, *Adv. Mater.* **2013**, *25*, 4267.

[6]   H. Seo, S. Aihara, T. Watabe, H. Ohtake, T. Sakai, M. Kubota, N. Egami, T. Hiramatsu, T. Matsuda, M. Furuta, T. Hirao, *Jpn. J. Appl. Phys.* **2011**, *50*.

[7]   S.-J. Lim, D.-S. Leem, K.-B. Park, K.-S. Kim, S. Sul, K. Na, G. H. Lee, C.-J. Heo, K.-H. Lee, X. Bulliard, R.-I. Satoh, T. Yagi, T. Ro, D. Im, J. Jung, M. Lee, T.-Y. Lee, M. G. Han, Y. W. Jin, S. Lee, *Sci. Rep.* **2015**, *5*, 7708.

[8]   Z. Yang, T. Albrow-Owen, W. Cai, T. Hasan, *Science,* **2021**, *371*, eabe0722.

[9]   F. Verstraeten, S. Gielen, P. Verstappen, J. Raymakers, H. Penxten, L. Lutsen, K. Vandewal, W. Maes, *J. Mater. Chem. C* **2020**, *8*, 10098.

[10]   F. Verstraeten, S. Gielen, P. Verstappen, J. Kesters, E. Georgitzikis, J. Raymakers, D. Cheyns, P. Malinowski, M. Daenen, L. Lutsen, K. Vandewal, W. Maes, *J. Mater. Chem. C* **2018**, *6*, 11645.

[11]   S. Gielen, C. Kaiser, F. Verstraeten, J. Kublitski, J. Benduhn, D. Spoltore, P. Verstappen, W. Maes, P. Meredith, A. Armin, K. Vandewal, *Adv. Mater.* **2020**, *32*, 2003818.

[12]   J. H. Kim, A. Liess, M. Stolte, A. Krause, V. Stepanenko, C. Zhong, D. Bialas, F. Spano, F. Würthner, *Adv. Mater.* **2021**, *33*, 2100582.

[13]   A. Armin, R. D. Jansen-van Vuuren, N. Kopidakis, P. L. Burn, P. Meredith, *Nat. Commun.* **2015**, *6*, 6343.

[14] Z. Tang, Z. Ma, A. Sánchez-Díaz, S. Ullbrich, Y. Liu, B. Siegmund, A. Mischok, K. Leo, M. Campoy-Quiles, W. Li, K. Vandewal, *Adv. Mater.* **2017**, *29*, 1702184.

[15] Y. Wang, B. Siegmund, Z. Tang, Z. Ma, J. Kublitski, S. Xing, V. C. Nikolis, S. Ullbrich, Y. Li, J. Benduhn, D. Spoltore, K. Vandewal, K. Leo, *Adv. Opt. Mater.* **2021**, *9*, 2001784.

[16] J. Vanderspikken, W. Maes, K. Vandewal, *Adv. Funct. Mater.* **2021**, 2104060.

[17] C. Kaiser, K. S. Schellhammer, J. Benduhn, B. Siegmund, M. Tropiano, J. Kublitski, D. Spoltore, M. Panhans, O. Zeika, F. Ortmann, P. Meredith, A. Armin, K. Vandewal, *Chem. Mater.* **2019**, *31*, 9325.

[18] T. M. Burke, S. Sweetnam, K. Vandewal, M. D. McGehee, *Adv. Energy Mater.* **2015**, *5*, 1500123.

[19] K. Vandewal, K. Tvingstedt, A. Gadisa, O. Inganäs, J. V. Manca, *Nat. Mater.* **2009**, *8*, 904.

[20] B. Siegmund, A. Mischok, J. Benduhn, O. Zeika, S. Ullbrich, F. Nehm, M. Böhm, D. Spoltore, H. Fröb, C. Körner, K. Leo, K. Vandewal, *Nat. Commun.* **2017**, *8*, 15421.

[21] N. C. Cates, R. Gysel, Z. Beiley, C. E. Miller, M. F. Toney, M. Heeney, I. McCulloch, M. D. McGehee, *Nano Lett.* **2009**, *9*, 4153.

[22] N. C. Miller, E. Cho, R. Gysel, C. Risko, V. Coropceanu, C. E. Miller, S. Sweetnam, A. Sellinger, M. Heeney, I. McCulloch, J. L. Brédas, M. F. Toney, M. D. McGehee, *Adv. Energy Mater.* **2012**, *2*, 1208.

[23] J. Lee, S.-J. Ko, H. Lee, J. Huang, Z. Zhu, M. Seifrid, J. Vollbrecht, V. V. Brus, A. Karki, H. Wang, K. Cho, T.-Q. Nguyen, G. C. Bazan, *ACS Energy Lett.* **2019**, *4*, 1401.

[24] M. A. M. Leenen, T. Meyer, F. Cucinotta, H. Thiem, R. Anselmann, L. De Cola, *J. Polym. Sci. Part A Polym. Chem.* **2010**, *48*, 1973.

[25] M. Takahashi, K. Masui, H. Sekiguchi, N. Kobayashi, A. Mori, M. Funahashi, N. Tamaoki, *J. Am. Chem. Soc.* **2006**, *128*, 10930.

[26] K. Masui, H. Ikegami, A. Mori, *J. Am. Chem. Soc.* **2004**, *126*, 5074.

[27] I. McCulloch, M. Heeney, C. Bailey, K. Genevicius, I. MacDonald, M. Shkunov, D. Sparrowe, S. Tierney, R. Wagner, W. Zhang, M. L. Chabinyc, R. J. Kline, M. D. McGehee, M. F. Toney, *Nat. Mater.* **2006**, *5*, 328.

[28] K. Vandewal, K. Tvingstedt, A. Gadisa, O. Inganäs, J. V. Manca, *Phys. Rev. B* **2010**, *81*, 125204.

[29] R. A. Marcus, *J. Phys. Chem.* **1989**, *93*, 3078.

[30] N. C. Miller, R. Gysel, C. E. Miller, E. Verploegen, Z. Beiley, M. Heeney, I. McCulloch, Z. Bao, M. F. Toney, M. D. McGehee, *J. Polym. Sci. Part B Polym. Phys.* **2011**, *49*, 499.

[31] F. C. Jamieson, E. B. Domingo, T. McCarthy-Ward, M. Heeney, N. Stingelin, J. R. Durrant, *Chem. Sci.* **2012**, *3*, 485.

[32] A. C. Mayer, M. F. Toney, S. R. Scully, J. Rivnay, C. J. Brabec, M. Scharber, M. Koppe, M. Heeney, I. McCulloch, M. D. McGehee, *Adv. Funct. Mater.* **2009**, *19*, 1173.

[33] K. Tvingstedt, C. Deibel, *Adv. Energy Mater.* **2016**, *6*, 1502230.

[34] M. S. Ünlü, S. Strite, *J. Appl. Phys.* **1995**, *78*, 607.

[35] L. A. A. Pettersson, L. S. Roman, O. Inganäs, *J. Appl. Phys.* **1999**, *86*, 487.

[36] A. Armin, M. Hambsch, I. K. Kim, P. L. Burn, P. Meredith, E. B. Namdas, *Laser Photon. Rev.* **2014**, *8*, 924.

[37] Y. Fang, A. Armin, P. Meredith, J. Huang, *Nat. Photonics* **2019**, *13*, 1-4.

[38] Thorlabs, Calibrated photodiodes, https://www.thorlabs.com/newgrouppage9.cfm?objectgroup_id=2822, (accessed: April 2021).

[39] X. Gong, M. Tong, Y. Xia, W. Cai, J. S. Moon, Y. Cao, G. Yu, C. L. Shieh, B. Nilsson, A. J. Heeger, *Science,* **2009**, *325*, 1665.

[40] J. Tong, J. Li, P. Zhang, X. Ma, M. Wang, L. An, J. Sun, P. Guo, C. Yang, Y. Xia,

Polymer, **2017**, *121*, 183.

[41]   A.J. Bard, R. Faulkner, L., *Electrochemical methods: fundamentals and applications*,

Wiley, **2001**.

[42]   S. Trasatti, *Pure Appl. Chem.* **1986**, *58*, 955.

[43]   Q. Liu, L. G. Gerling, F. Bernal-Texca, J. Toudert, T. Li, X. Zhan, J. Martorell, *Adv.*

Energy Mater. **2020**, *10*, 1904196.

Significant extention of the direct charge-transfer absorption to longer wavelengths of the well-known PBTTT:PC$_{61}$BM blend through polymer side chain engineering is demonstrated. When applied into an optical cavity device, the novel intercalating blend extends its employability for NIR detection by more than 300 nm.
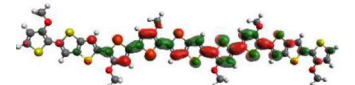
Jochen Vanderspikken, Quan Liu*, Zhen Liu, Tom Vandermeeren, Tom Cardeynaels, Sam Gielen, Bruno Van Mele, Niko Van den Brande, Benoît Champagne, Koen Vandewal*, Wouter Maes*

Tuning electronic and morphological properties for high-performance wavelength-selective organic near-infrared cavity photodetectors
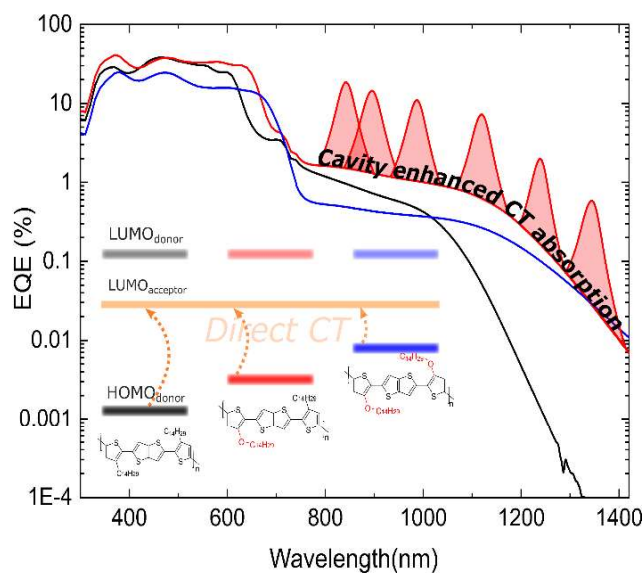
Supporting Information

Tuning electronic and morphological properties for high-performance wavelength-selective organic near-infrared cavity photodetectors
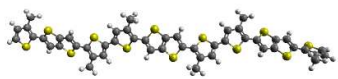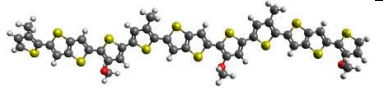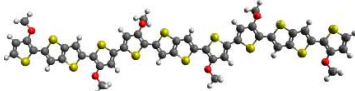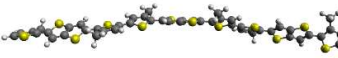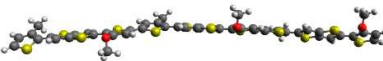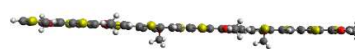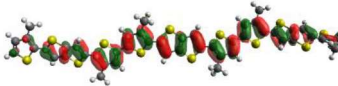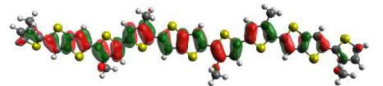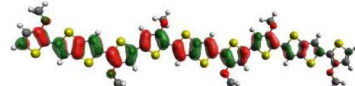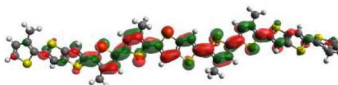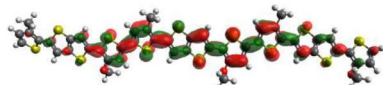
Jochen Vanderspikken, Quan Liu*, Zhen Liu, Tom Vandermeeren, Tom Cardeynaels, Sam Gielen, Bruno Van Mele, Niko Van den Brande, Benoît Champagne, Koen Vandewal*, Wouter Maes*

## 1. Materials and methods

Theoretical calculations

Density functional theory (DFT) calculations were carried out using Gaussian 16[1] with the M06 exchange-correlation functional and the 6-311G(d) basis set.[2] For the PBTTT polymer and the novel PBTTT-OR-R and PBTTT-(OR)$_2$ variants, an alternating orientation between the thiophene units was chosen.

Table S1: Overview of the geometry and the frontier orbital energy levels for PBTTT, PBTTT-OR-R and PBTTT-(OR)$_2$ as obtained by DFT(M06/6-311G(d)). Isocontour values of 0.02 a.u. were used for all orbitals.

PBTTT	PBTTT-OR-R	PBTTT-(OR)$_2$
Geometry		
HOMO		
–4.952 eV	–4.883 eV	–4.580 eV
LUMO		
–2.044 eV	–2.095 eV	–2.037 eV

## Materials synthesis and characterization

2-bromo-3-tetradecylthiophene (Th-R)
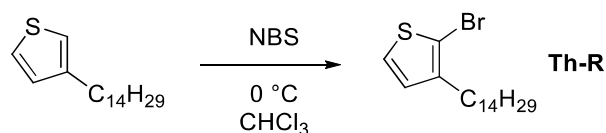
3-Tetradecylthiophene (5.00 g, 17.8 mmol, 1 eq) was dissolved in dry THF (50 mL). The solution was cooled to 0 °C and NBS powder (3.17 g, 17.8 mmol, 1 eq) was added in two portions, 30 min apart. The reaction mixture was stirred and allowed to steadily reach room temperature overnight (~15 h). The mixture was quenched in water and diethyl ether was added. The organic layer was washed 3x with water, dried over $MgSO_4$ and filtered. Solvents were removed by evaporation and the resulting yellow oil was purified by silica flash chromatography using petroleum ether as the eluent. A colorless oil was obtained (6.54 g, quantitative yield).

^{1}H NMR (400 MHz, CDCl$_3$) δ 7.18 (d, J = 5.6 Hz, 1H), 6.79 (d, J = 5.6 Hz, 1H), 2.56 (t, J = 7.1 Hz, 2H), 1.58 (q, J = 7.5 Hz, 2H), 1.32 − 1.29 (m, 22H), 0.88 (t, J = 6.8 Hz, 3H). ^{13}C NMR (100 MHz, CDCl$_3$) δ 142.1, 128.4, 125.3, 108.9, 32.1, 29.9, 29.8, 29.6, 29.5, 29.4, 22.9, 14.3.

3-(tetradecyloxy)thiophene (A)
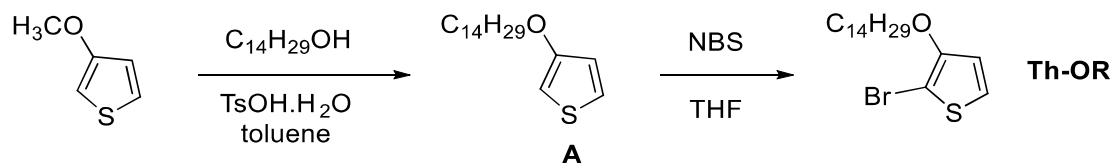
3-Methoxythiophene (5.00 g, 43.8 mmol, 1 eq), 1-tetradecanol (18.78 g, 87.6 mmol, 2 eq) and *p*-toluenesulfonic acid monohydrate (0.83 g, 4.38 mmol, 0.1 eq) were dissolved in toluene (100 mL) and the mixture was heated to reflux for 20 h. Subsequently, the reaction mixture was poured into water, extracted with toluene, dried over $MgSO_4$ and filtered. Solvents were

evaporated and the resulting crude product was subjected to kügelrohr distillation to remove the residual 1-tetradecanol. A dark green solid was obtained (9.80 g, 75%).

^{1}H NMR (400 MHz, CDCl$_3$) δ 7.16 (dd, J = 5.2, 3.1 Hz, 1H), 6.75 (dd, J = 5.2, 1.5 Hz, 1H), 6.22 (dd, J = 3.1, 1.5 Hz, 1H), 3.94 (t, J = 6.6 Hz, 2H), 1.82 – 1.72 (m, 2H), 1.50 – 1.39 (m, 2H), 1.38 – 1.20 (m, 20H), 0.88 (t, J = 6.8 Hz, 3H). ^{13}C NMR (100 MHz, CDCl$_3$) δ 158.2, 124.6, 119.7, 97.0, 70.4, 32.1, 29.8, 29.8, 29.7, 29.6, 29.5, 29.4, 26.2, 22.9, 14.3.

2-bromo-3-(tetradecyloxy)thiophene (Th-OR)

3-Tetradecyloxythiophene (4.00 g, 13.5 mmol, 1 eq) was dissolved in dry THF (30 mL). The solution was cooled to 0 °C and NBS powder (2.40 g, 13.5 mmol, 1 eq) was added in two portions, 30 min apart. The reaction mixture was stirred and allowed to steadily reach room temperature overnight (~15 h). The mixture was quenched in water and dichloromethane was added. The organic layer was washed 3x with water, dried over MgSO$_4$ and filtered. Solvents were removed by evaporation and the resulting yellow oil was purified by silica flash chromatography using petroleum ether:dichloromethane (95:5) as the eluent mixture. A yellow solid was obtained (4.43 g, 87%).

^{1}H NMR (400 MHz, CDCl$_3$) δ 7.18 (d, J = 5.9 Hz, 1H), 6.74 (d, J = 5.9 Hz, 1H), 4.03 (t, J = 6.6 Hz, 2H), 1.81 – 1.68 (m, 2H), 1.49 – 1.39 (m, 2H), 1.38 – 1.20 (m, 20H), 0.88 (t, J = 6.8 Hz, 3H). ^{13}C NMR (100 MHz, CDCl$_3$) δ 154.7, 124.3, 117.6, 91.6, 72.4, 32.1, 29.8, 29.7, 29.7, 29.6, 29.5, 29.5, 26.0, 22.9, 14.3.

5,5'-dibromo-4,4'-ditetradecyl-2,2'-bithiophene (BiT-R₂), 5,5'-dibromo-4-tetradecyl-4'-(tetradecyloxy)-2,2'-bithiophene (BiT-OR-R) and 5,5'-dibromo-4,4'-bis(tetradecyloxy)-2,2'-bithiophene (BiT-(OR)₂)
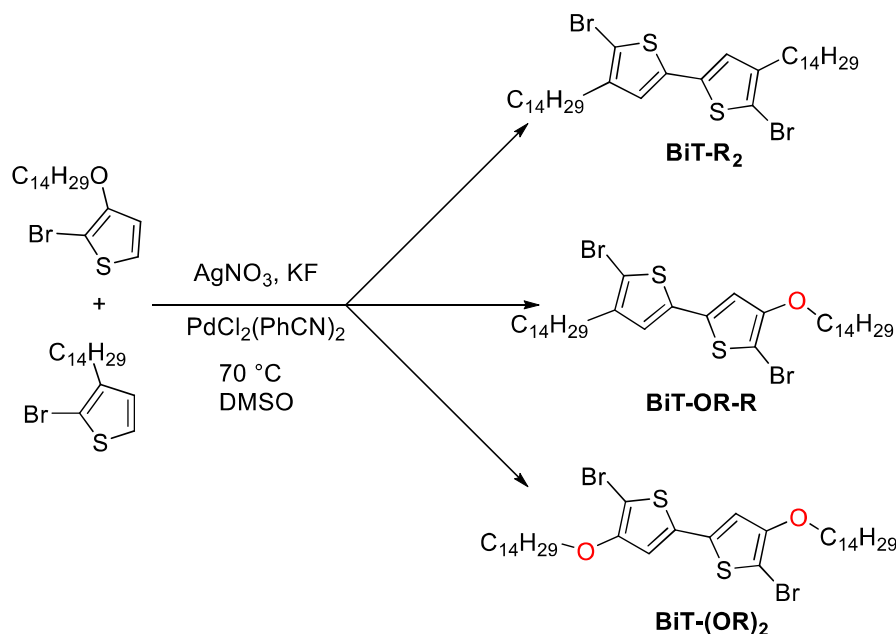
In the absence of light, KF (0.161 g, 2.78 mmol, 4 eq) and AgNO$_3$ (0.473 g, 2.78 mmol, 4 eq) were added to a solution of 2-bromo-3-tetradecylthiophene (0.250 g, 0.696 mmol, 1 eq) and 2-bromo-3-(tetradecyloxy)thiophene (0.261 g, 0.696 mmol, 1 eq) in dry DMSO (30 mL). After addition of PdCl$_2$(PhCN)$_2$ (5.3 mg, 0.014 mmol, 0.02 eq), the mixture was stirred at 70 °C for 6 h. The same amounts of KF, AgNO$_3$ and PdCl$_2$(PhCN)$_2$ were added a second time and after 14 h a third time, and the mixture was stirred for another 5 h. Subsequently, the mixture was allowed to reach room temperature and it was filtered over celite. The celite cake was washed multiple times with dichloromethane. The red-brown filtrate was washed three times with demineralised water, dried over MgSO$_4$, filtered and the solvent was evaporated. The obtained brown solid was purified through column chromatography starting with *n*-hexane and gradually increasing polarity with dichloromethane. The three coupled bithiophene products (**BiT-R₂**, **BiT-OR-R** and **BiT-OR₂**) were isolated as yellow solids.

5,5'-dibromo-4,4'-ditetradecyl-2,2'-bithiophene (BiT-R₂): 101 mg, 20%

^{1}H NMR (400 MHz, CDCl₃) δ 6.77 (s, 2H), 2.51 (t, *J* = 7.5 Hz, 4H), 1.62 – 1.50 (m, 4H), 1.37 – 1.20 (m, 44H), 0.88 (t, *J* = 6.7 Hz, 6H). ^{13}C NMR (100 MHz, CDCl₃) δ 143.1, 136.3, 124.6, 108.0, 32.1, 29.8, 29.7, 29.5, 29.3, 22.9, 14.3.
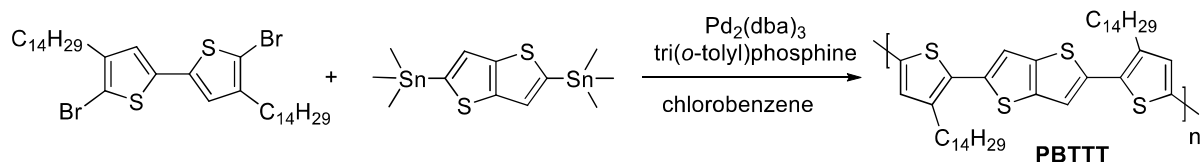
5,5'-dibromo-4-tetradecyl-4'-(tetradecyloxy)-2,2'-bithiophene (BiT-OR-R): 138 mg, 27%

^{1}H NMR (400 MHz, CDCl₃) δ 6.79 (s, 1H), 6.72 (s, 1H), 4.04 (t, *J* = 6.6 Hz, 2H), 2.55 – 2.48 (m, 2H), 1.81 – 1.71 (m, 2H), 1.62 – 1.52 (m, 2H), 1.50 – 1.39 (m, 2H), 1.38 – 1.20 (m, 42H), 0.88 (t, *J* = 6.6 Hz, 6H). ^{13}C NMR (100 MHz, CDCl₃) δ 154.9, 143.6, 136.8, 135.2, 124.8, 114.1, 108.6, 91.0, 72.8, 32.4, 30.1, 30.1, 30.0, 29.9, 29.8, 29.8, 29.7, 26.3, 23.2, 14.6.

5,5'-dibromo-4,4'-bis(tetradecyloxy)-2,2'-bithiophene (BiT-(OR)₂): 100 mg, 20%

^{1}H NMR (400 MHz, CDCl₃) δ 6.73 (s, 2H), 4.04 (t, *J* = 6.6 Hz, 4H), 1.81 – 1.71 (m, 4H), 1.50 – 1.40 (m, 4H), 1.38 – 1.21 (m, 40H), 0.88 (t, *J* = 6.7 Hz, 6H). ^{13}C NMR (100 MHz, CDCl₃) δ 154.7, 144., 135.01, 113.6, 91.0, 72.6, 32.1, 29.8, 29.8, 29.7, 29.7, 29.6, 29.5, 29.5, 25.9, 22.9, 14.3.

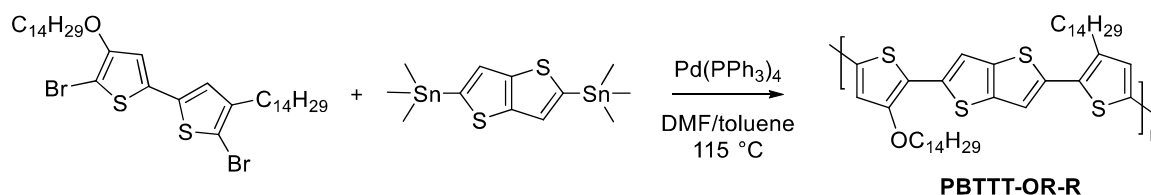*poly(2,5-bis(3-tetradecylthiophen-2-yl)thieno[3,2-b]thiophene) (PBTTT)*[3]

A 20 mL microwave glass vial was charged with a stirring bar, 5,5'-dibromo-4,4'-ditetradecyl-2,2'-bithiophene (200.0 mg, 279 μmol), 2,5-bis(trimethylstannyl)thieno[3,2-*b*]thiophene (130.0 mg, 279 μmol), tris(dibenzylideneacetone)dipalladium (0) (6.39 mg, 2.5 mol%), tri(*o*-tolyl)phosphine (8.49 mg, 10 mol%) and chlorobenzene (4.7 mL). The glass vial was purged with nitrogen, securely sealed and heated in a microwave reactor. A temperature ramp was used: the vial was heated while stirring at 140 °C for 120 s, then at 160 °C for 120 s and finally

at 180 °C for 900 s. The elapsed time was only calculated once the temperature had been reached. The mixture was diluted with chlorobenzene, the Pd scavenger diethylammonium diethyldithiocarbamate was added and the mixture was stirred for 2 h at 115 °C. Subsequently, the hot mixture was added to methanol. The precipitate was subjected to soxhlet extraction with methanol (1 h), acetone (1 h), hexanes (3 h), chloroform (4 h) and chlorobenzene (12 h). The chloroform and chlorobenzene fractions were once again precipitated in methanol, filtered off and dried under high vacuum. This resulted in 139 mg from the chloroform fraction (which was used in the further studies) and 30 mg from the chlorobenzene fraction, affording a total of 169 mg (87%).

SEC (1,2,4-trichlorobenzene, 160 °C, PS standards): $M_{n\,CHCl3}$: 13.2 kg/mol, $Đ_{CHCl3}$: 1.8; $M_{n\,CB}$: 37.6 kg/mol, $Đ_{CHCl3}$: 1.4

UV-Vis-NIR: $\lambda_{max,film}$: 529 nm

poly(2-(3-(tetradecyloxy)thiophen-2-yl)-5-(3-tetradecylthiophen-2-yl)thieno[3,2-b]thiophene) (PBTTT-OR-R)
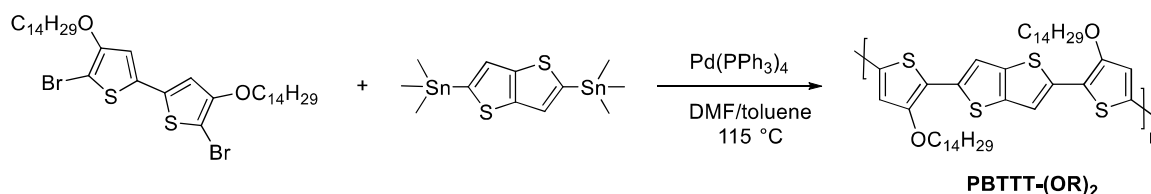

PBTTT-OR-R

A schlenk tube was charged with a stirring bar, 5,5'-dibromo-4-tetradecyl-4'-(tetradecyloxy)-2,2'-bithiophene (312.5 mg, 426.4 µmol), 2,5-bis(trimethylstannyl)thieno[3,2-*b*]thiophene (198.6 mg, 426.4 µmol), tetrakis(triphenylphosphine)palladium(0) (12.3 mg, 2.5 mol %) and degassed DMF:toluene (3.6:5.5 mL). The reaction vessel was subjected 5x to a vacuum-N_2 cycle and then heated to 115 °C for 48 h. The mixture was diluted with chlorobenzene, the Pd scavenger diethylammonium diethyldithiocarbamate was added and the mixture was stirred for 2 h at 115 °C. Subsequently, the hot mixture was added to methanol. The precipitate was subjected to soxhlet extraction with methanol (2 h), acetone (2 h), hexanes (3 h),

dichloromethane (3 h), chloroform (24 h) and chlorobenzene (24 h). The dichloromethane, chloroform and chlorobenzene fractions were once again precipitated in methanol, filtered off and dried under high vacuum. This resulted in 108 mg from the dichloromethane fraction, 122 mg from the chloroform fraction (which was used in the further studies) and 24 mg from the chlorobenzene fraction, affording a total of 254 mg (86%).

SEC (1,2,4-trichlorobenzene, 160 °C, PS standards): $M_{n\,DCM}$: 19.2 kg/mol, $Đ_{DCM}$: 1.4; $M_{n\,CHCl3}$: 42.4 kg/mol, $Đ_{CHCl3}$: 1.8; $M_{n\,CB}$: 81.1 kg/mol, $Đ_{CB}$: 1.9

UV-Vis-NIR: $\lambda_{max,film}$: 572 nm

poly(2,5-bis(3-tetradecyloxythiophen-2-yl)thieno[3,2-b]thiophene) (PBTTT-(OR)₂)

A schlenk tube was charged with a stirring bar, 5,5'-dibromo-4,4'-bis(tetradecyloxy)-2,2'-bithiophene (156.0 mg, 208 µmol), 2,5-bis(trimethylstannyl)thieno[3,2-*b*]thiophene (97.1 mg, 208 µmol), tetrakis(triphenylphosphine)palladium(0) (6.0 mg, 2.5 mol %) and degassed DMF:toluene (2:3 mL). The reaction vessel was subjected 5x to a vacuum-N_2 cycle and heated to 115 °C for 72 h. The mixture was diluted with chlorobenzene, the Pd scavenger diethylammonium diethyldithiocarbamate was added and the mixture was stirred for 2 h at 115 °C. Subsequently, the hot mixture was added to methanol. The precipitate was subjected to soxhlet extraction with methanol (2 h), acetone (1 h), hexanes (1 h), dichloromethane (2 h), chloroform (2 h) and chlorobenzene (12 h). The chloroform and chlorobenzene fractions were once again precipitated in methanol, filtered off and dried under high vacuum. This resulted in 47 mg from the dichloromethane fraction, 43 mg from the chloroform fraction (which was used in the further studies) and 9 mg from the chlorobenzene fraction, affording a total of 99 mg (65%).

SEC (1,2,4-trichlorobenzene, 160 °C, PS standards): $M_{n\ DCM}$: 11.4 kg/mol, $Đ_{DCM}$: 1.6; $M_{n\ CHCl3}$:

26.2 kg/mol, $Đ_{CHCl3}$: 2.2; $M_{n\ CB}$: 36.0 kg/mol, $Đ_{CB}$: 3.2

UV-Vis-NIR: $\lambda_{max,film}$: 614 nm

Table S2: Molar mass, electrochemical, optical, and thermal stability characteristics of PBTTT and the novel PBTTT-OR-R and PBTTT-(OR)$_2$ polymers.

Polymer[a]	M_n	M_w	Đ	HOMO$_{exp}$ (HOMO$_{calc}$)	LUMO$_{exp}$ (LUMO$_{calc}$)	λ_{max}	λ_{onset}	T_{degr}[b]
	[kg/mol]	[kg/mol]		[eV]		[nm]	[nm]	[°C]
PBTTT	13.2	23.2	1.8	−5.12 (−4.95)	−2.76 (−2.04)	529	639	356
PBTTT-OR-R	42.4	74.2	1.8	−4.87 (−4.88)	−2.75 (−2.10)	580	675	350
PBTTT-(OR)$_2$	26.2	58.5	2.2	−4.70 (−4.58)	−2.77 (−2.04)	603	718	316

[a] All characterization was done on the polymer samples obtained after soxhlet extraction in chloroform. [b] Onset of degradation as determined by 1% weight loss via TGA.
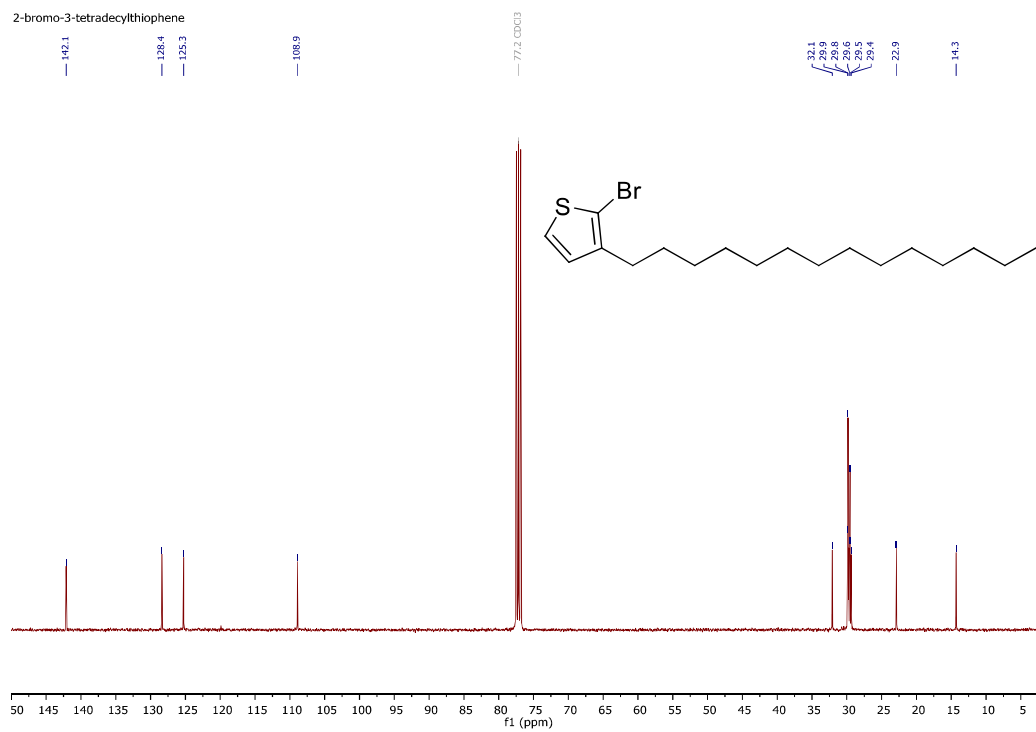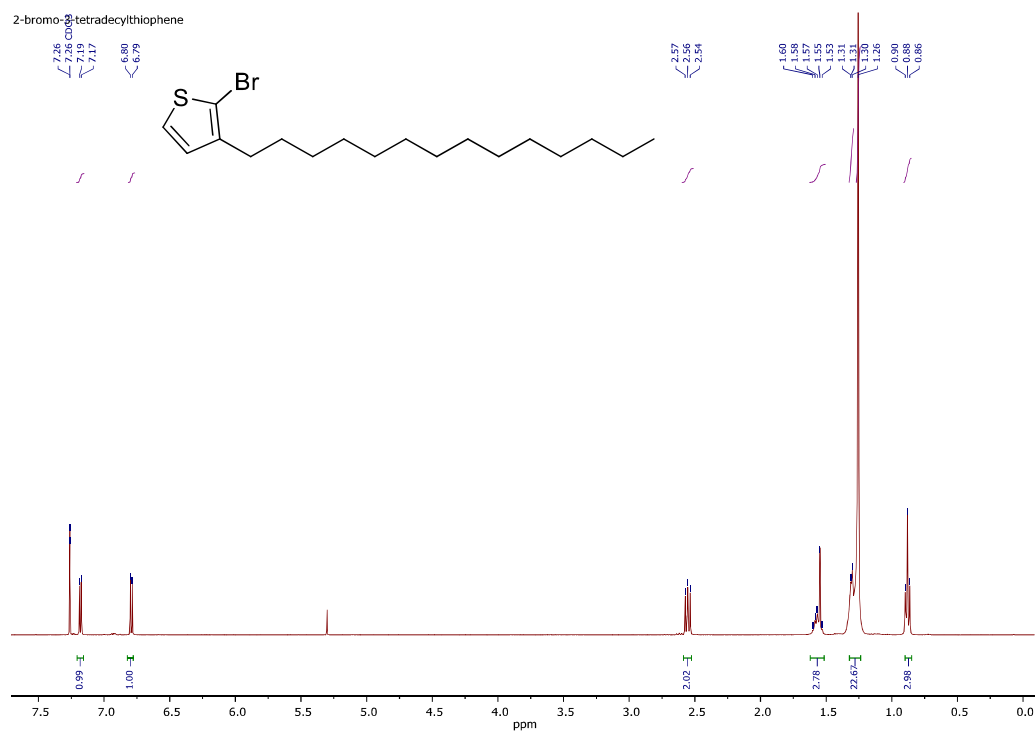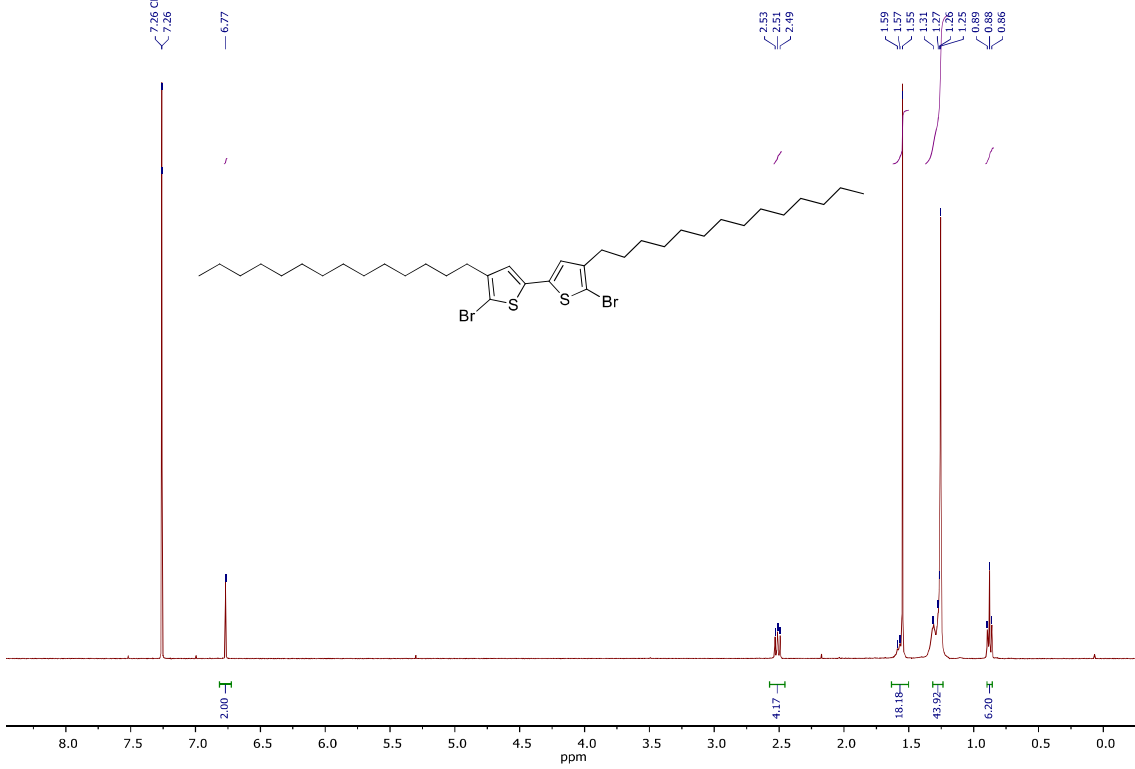
NMR spectra

2,5-bis(trimethylstannyl)thieno[3,2-b]thiophene

2,5-bis(trimethylstannyl)thieno[3,2-b]thiophene

S9
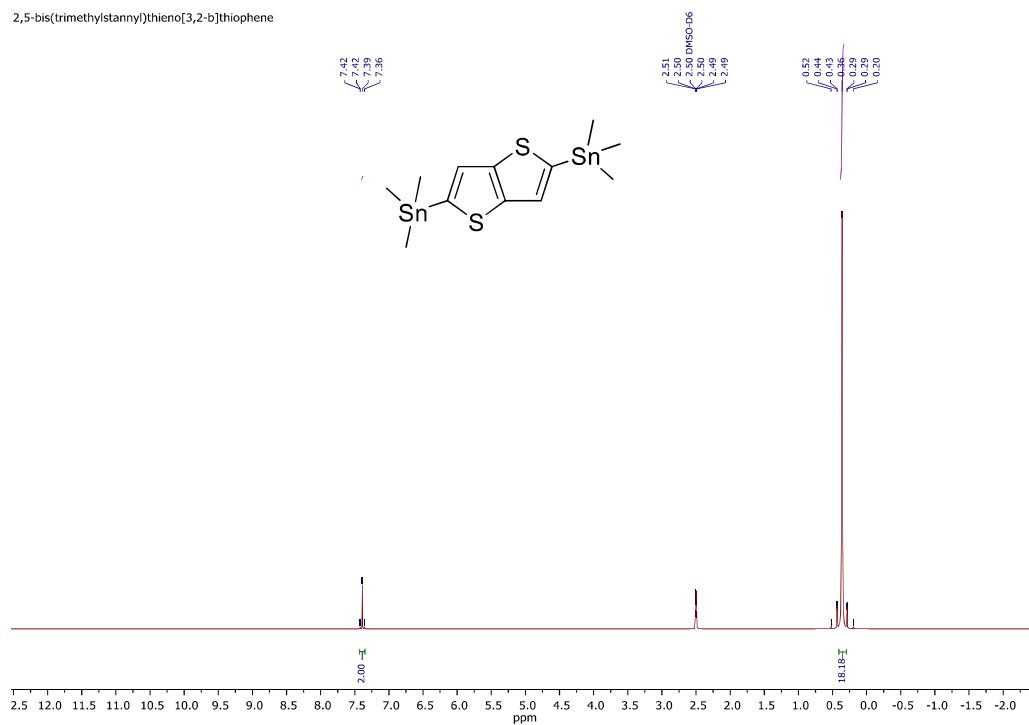
2-bromo-3-tetradecylthiophene
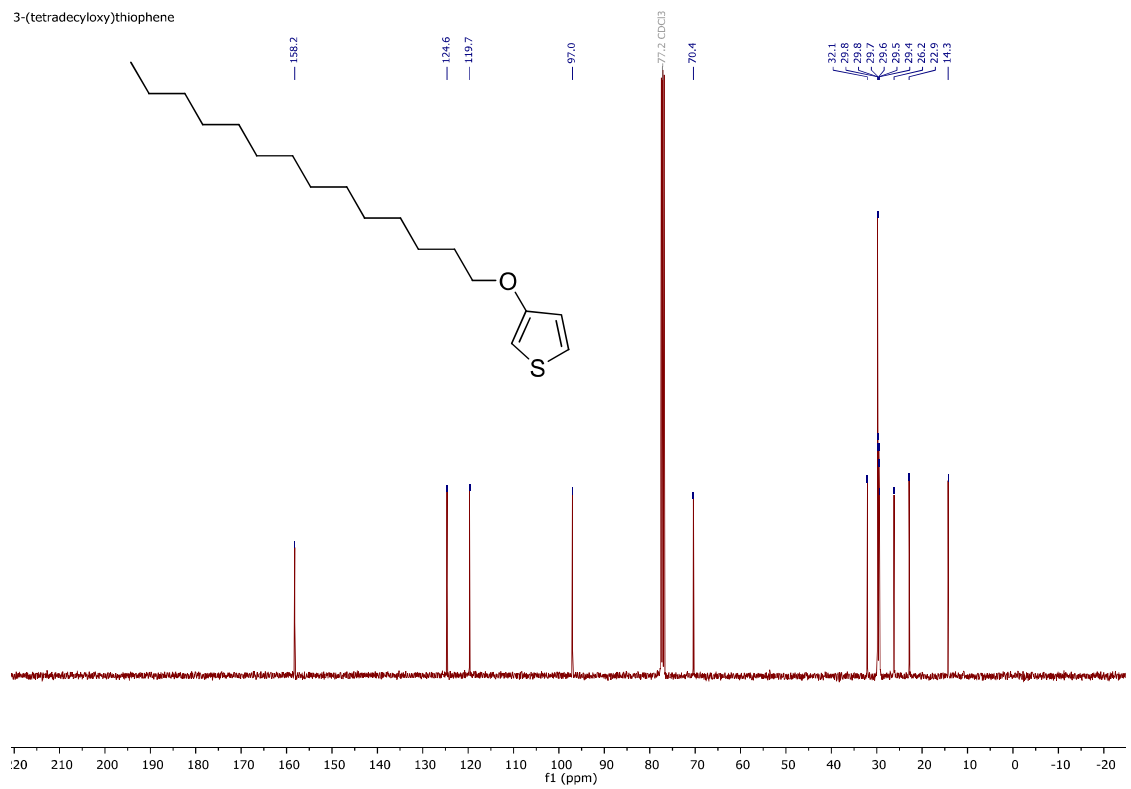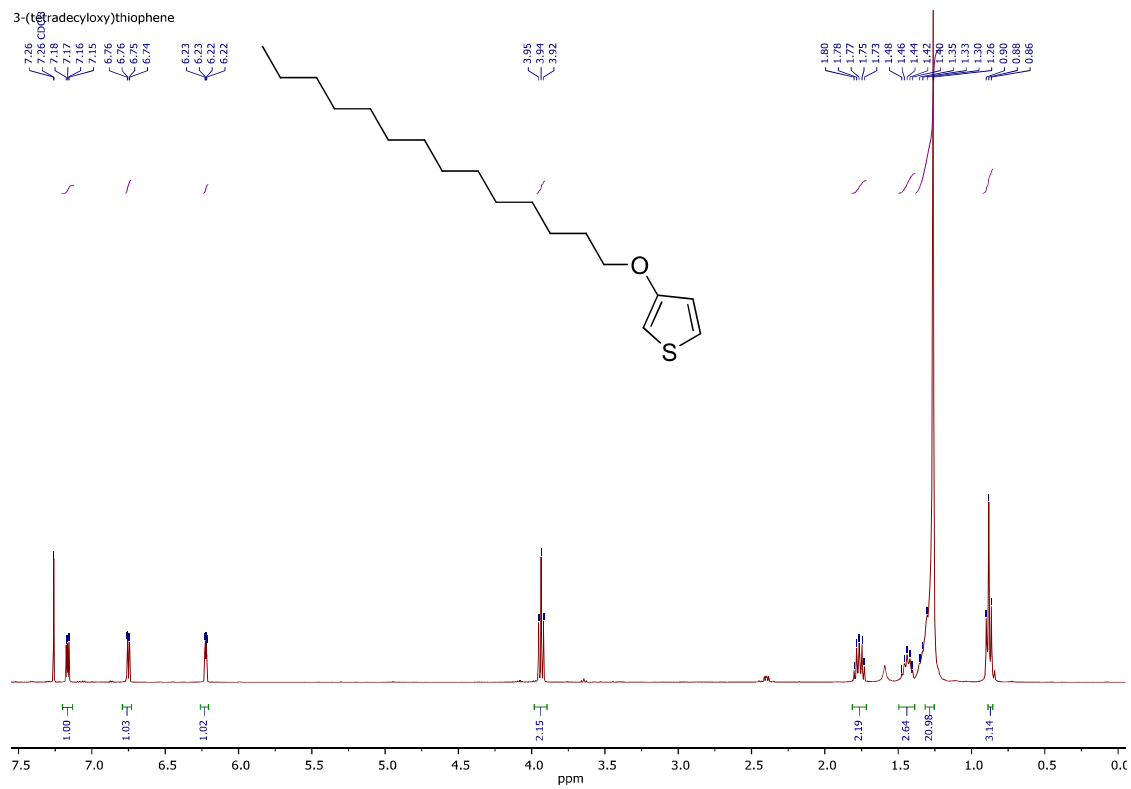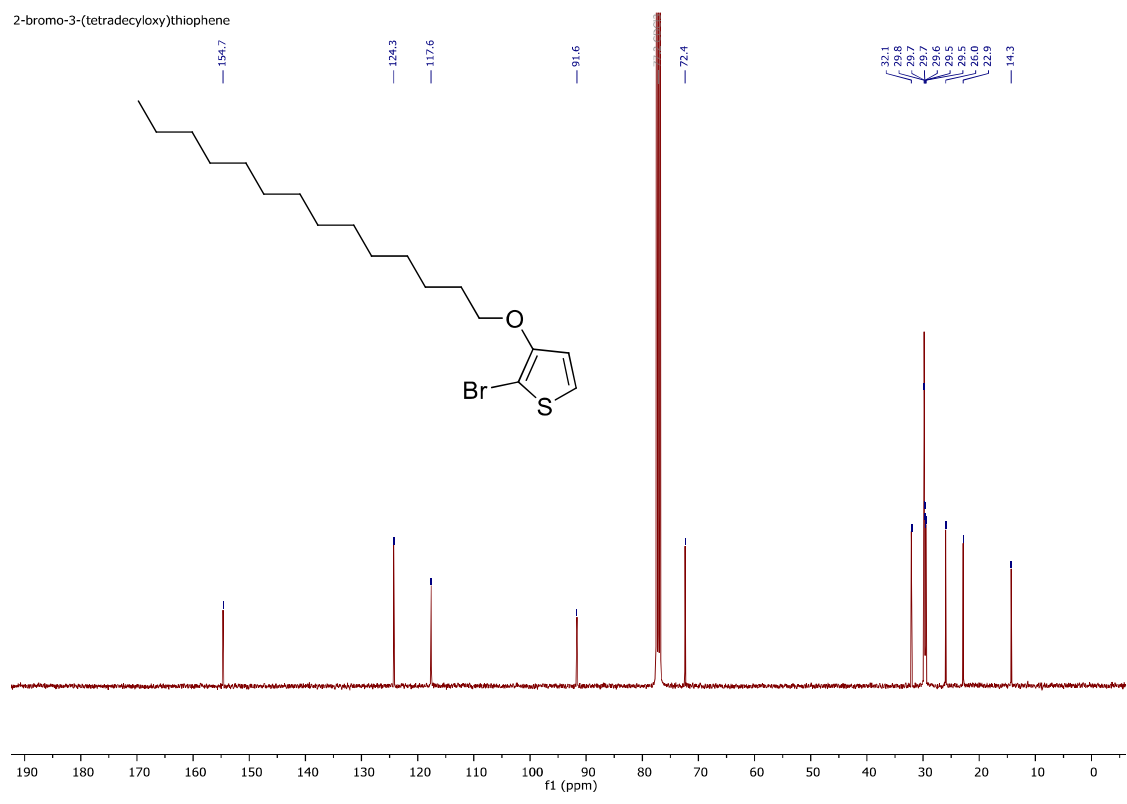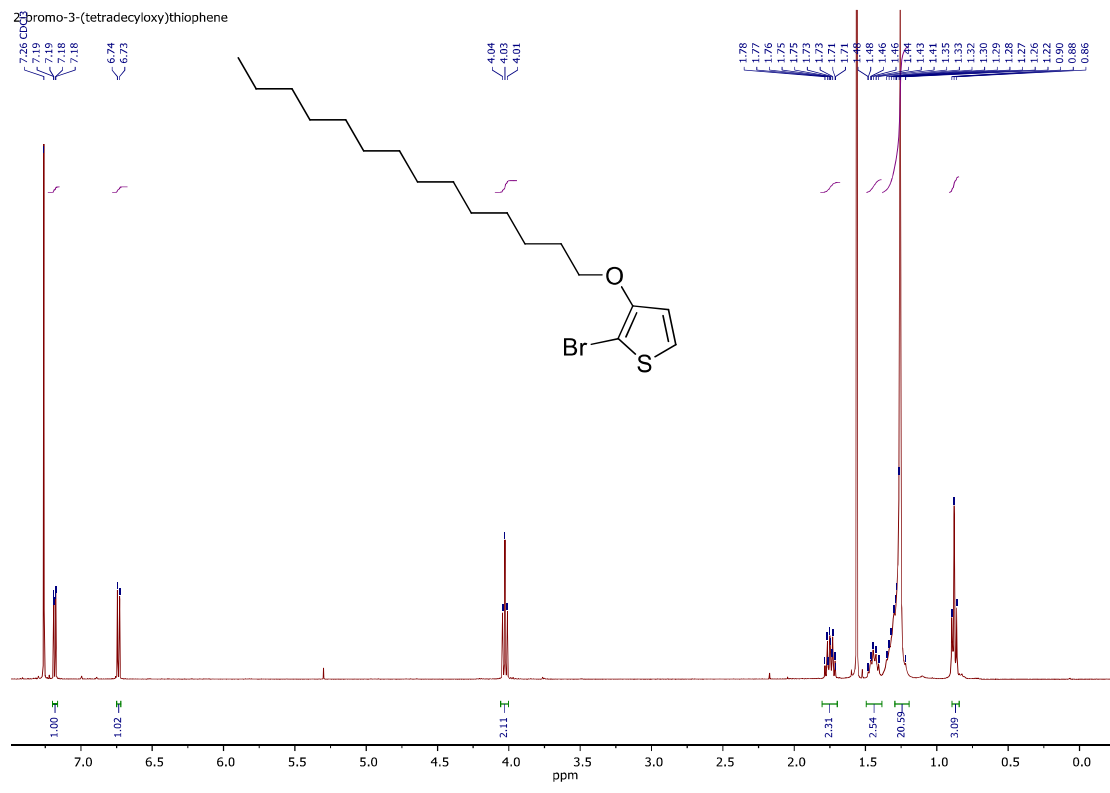

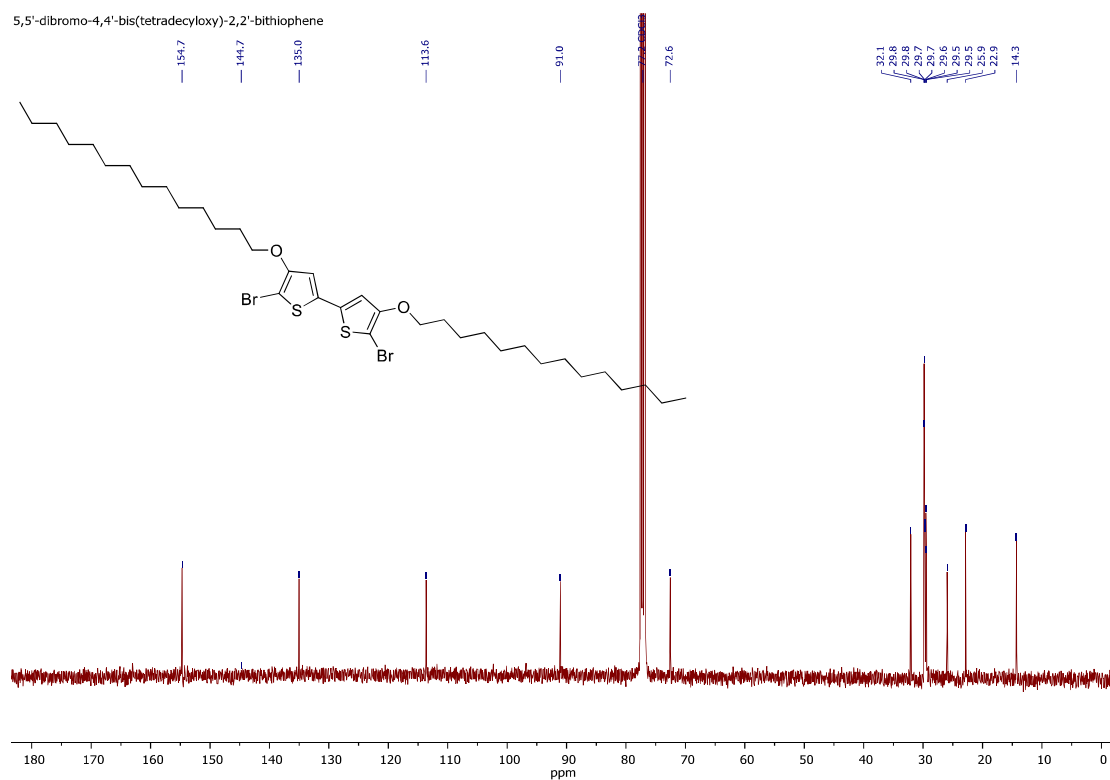2-bromo-3-tetradecylthiophene
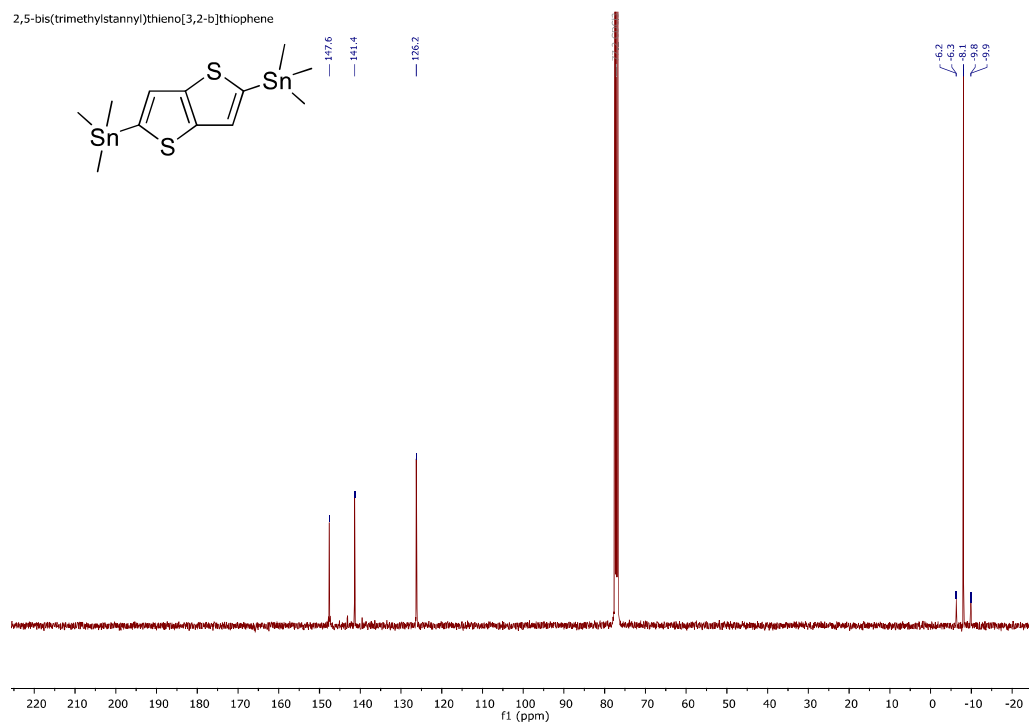
5,5'-dibromo-4,4'-ditetradecyl-2,2'-bithiophene

5,5'-dibromo-4,4'-ditetradecyl-2,2'-bithiophene carbon
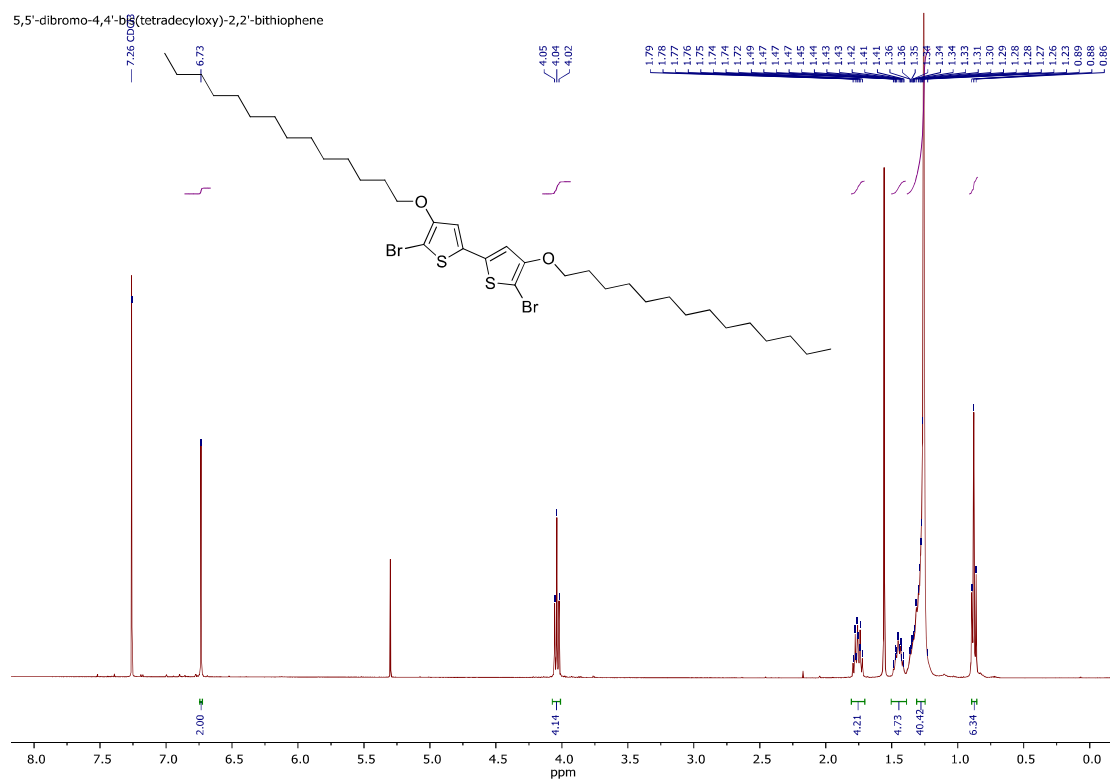
3-(tetradecyloxy)thiophene

3-(tetradecyloxy)thiophene

S12

2-bromo-3-(tetradecyloxy)thiophene

7.26 CDCl3
7.19
7.18
7.18
6.74
6.73
4.04
4.03
4.01
1.78
1.77
1.76
1.75
1.73
1.71
1.48
1.46
1.46
1.43
1.41
1.35
1.33
1.32
1.30
1.29
1.28
1.27
1.26
1.22
0.90
0.88
0.86

1.00
1.02
2.11
2.31
2.54
20.59
3.09

7.0 6.5 6.0 5.5 5.0 4.5 4.0 3.5 3.0 2.5 2.0 1.5 1.0 0.5 0.0
ppm

2-bromo-3-(tetradecyloxy)thiophene

154.7
124.3
117.6
91.6
72.4
32.1
29.8
29.7
29.6
29.5
29.5
26.0
22.9
14.3

190 180 170 160 150 140 130 120 110 100 90 80 70 60 50 40 30 20 10 0
f1 (ppm)

S13

5,5'-dibromo-4,4'-bis(tetradecyloxy)-2,2'-bithiophene

5,5'-dibromo-4,4'-bis(tetradecyloxy)-2,2'-bithiophene
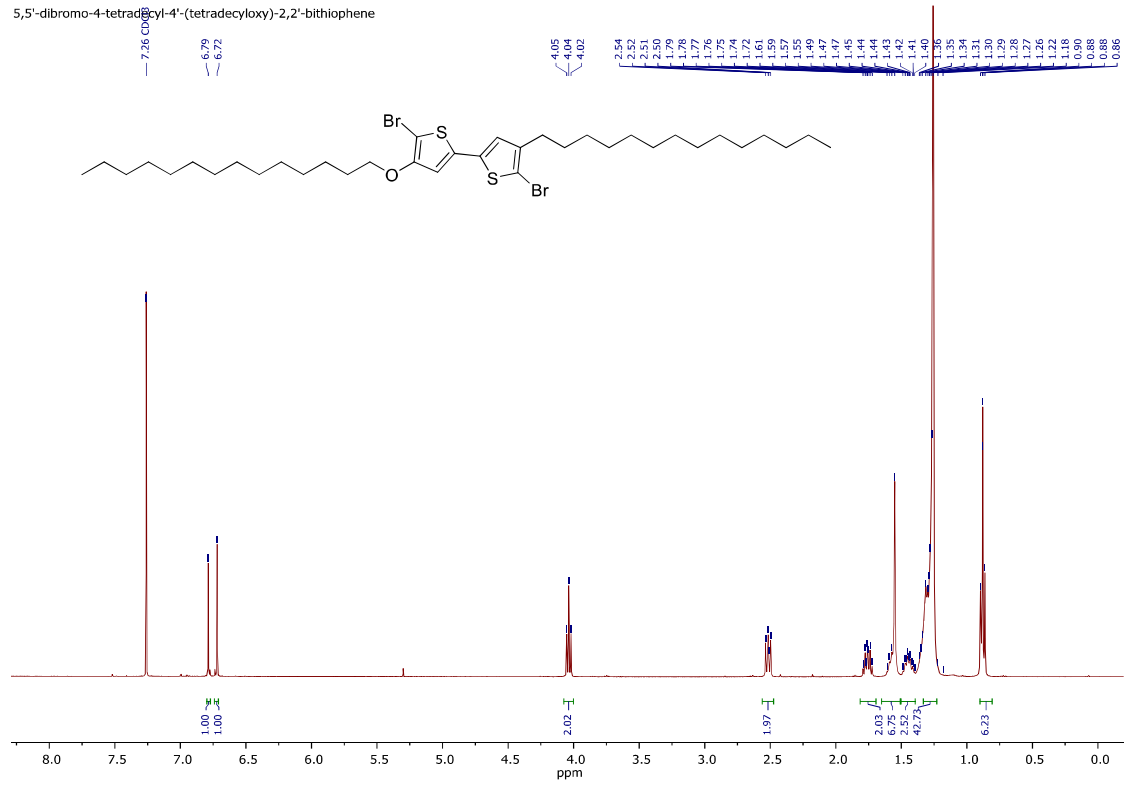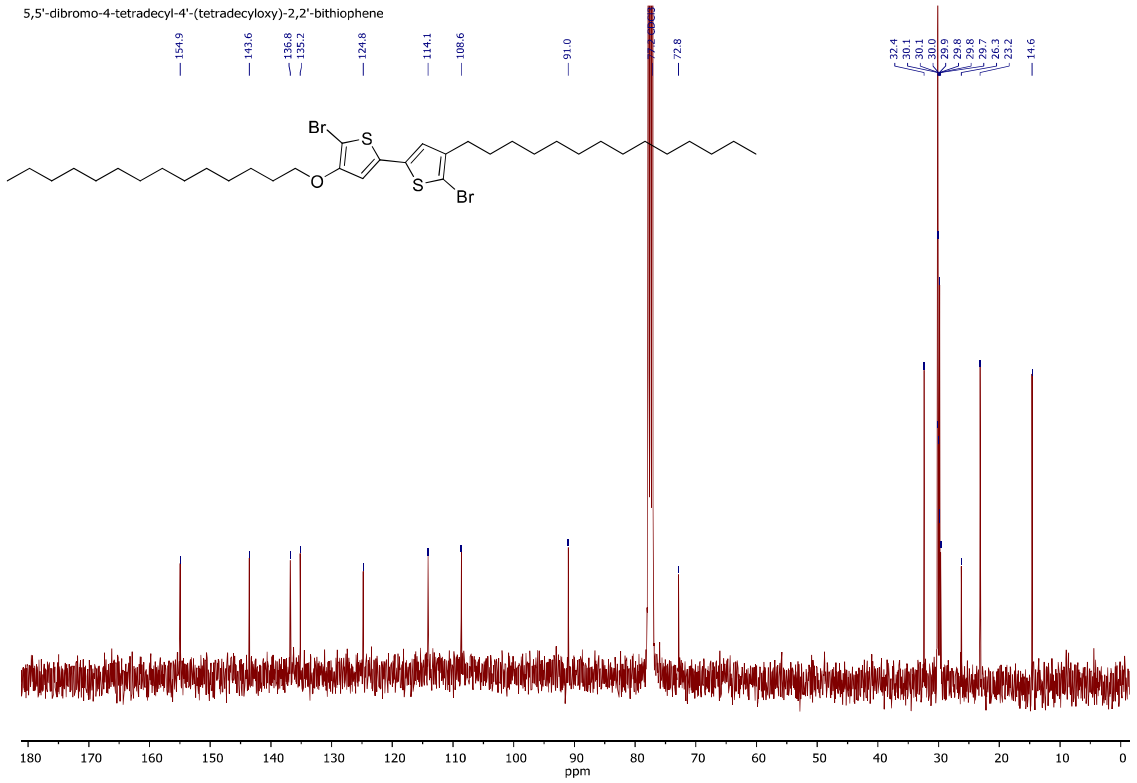

S14

5,5'-dibromo-4-tetradecyl-4'-(tetradecyloxy)-2,2'-bithiophene

5,5'-dibromo-4-tetradecyl-4'-(tetradecyloxy)-2,2'-bithiophene

S15

Determination of E_{CT}

In order to determine E_{CT} a fitting procedure was applied on the low energy tail of the sensitively measured EQE(E) spectrum, using the following equation, adapted from ref. [4]:

$$EQE(E) \sim \exp\left(-\frac{(E - \lambda - E_{CT})^2}{4\lambda k_B T}\right)$$

with λ being the reorganization energy, k_B the Boltzmann constant and T the temperature, in this case room temperature, making $k_B T$ equal to 0.025. In order to reliably take into account the low energy part of the spectrum, the fitting was done on the natural logarithm of the EQE(E) spectrum. The following fitting values are obtained:

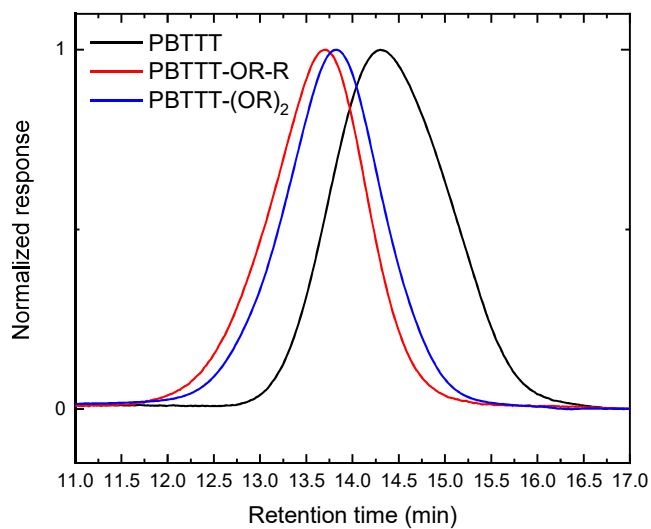|	E_{CT} (eV)	λ (eV)
PBTTT:PC$_{61}$BM	1.15	0.14
PBTTT-OR-R:PC$_{61}$BM	0.98	0.2
PBTTT-(OR)$_2$:PC$_{61}$BM	0.89	0.3

2. Supporting figures and tables

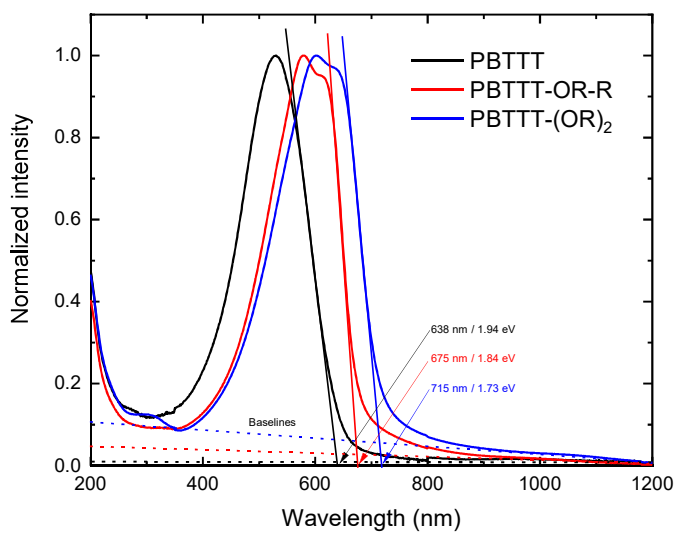**Figure S1:** Normalized GPC traces for the PBTTT polymer series.

Figure S2: UV-Vis-NIR absorption spectra for films of PBTTT, PBTTT-OR-R and PBTTT-(OR)$_2$, with the corresponding absorption onsets.
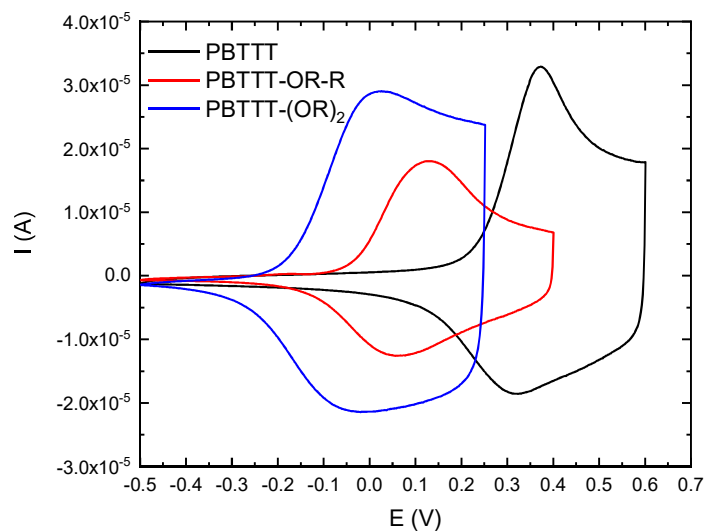
Figure S3: Overlay of the oxidation curves obtained via cyclic voltammetry for the PBTTT polymer series.
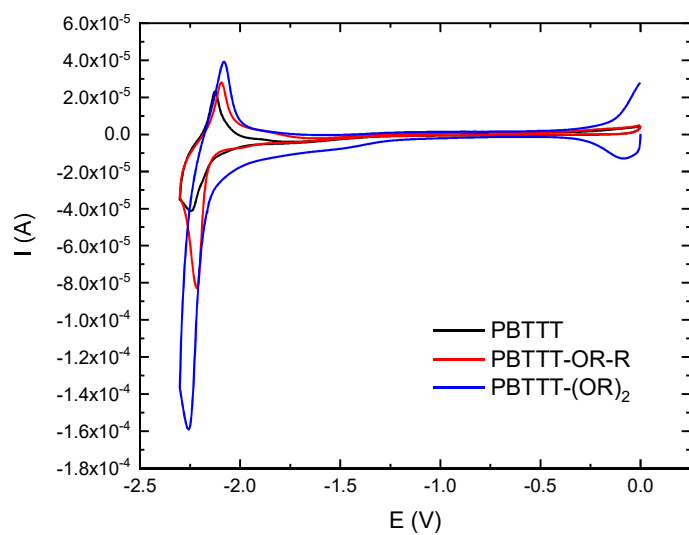

Figure S4: Overlay of the reduction curves obtained via cyclic voltammetry for the PBTTT polymer series.
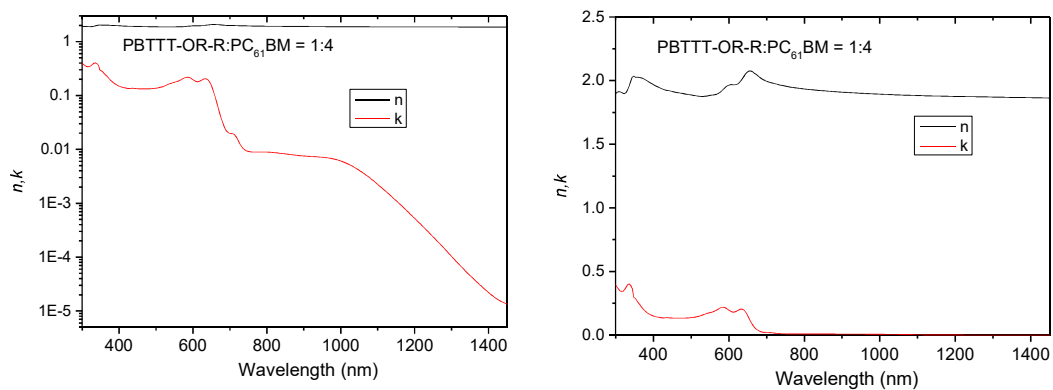
Figure S5: Refractive index (*n*) and extinction coefficient (*k*) for a PBTTT-OR-R:PC$_{61}$BM (1:4) blend on a logarithmic (left) and a linear (right) scale.
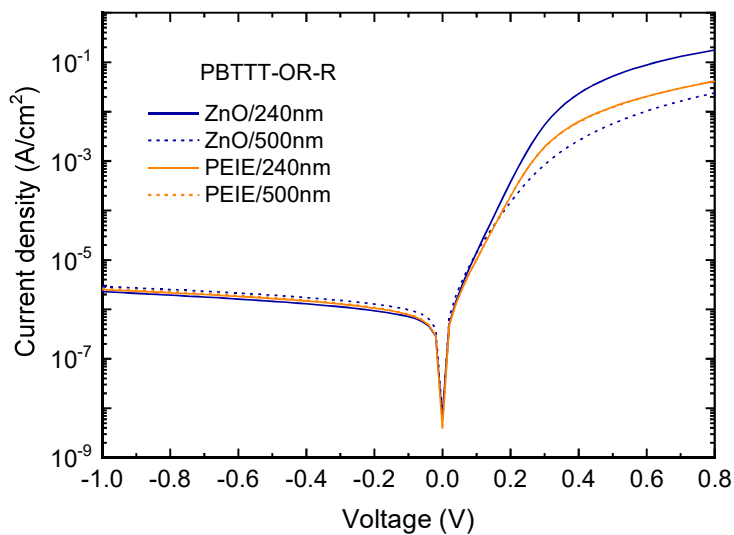
Figure S6 Influence of interlayers and their thickness on the dark current behavior (stack: glass/ITO/ZnO or PEIE/PBTTT-OR-R:PC$_{61}$BM (1:4)/MoO$_3$/Ag).
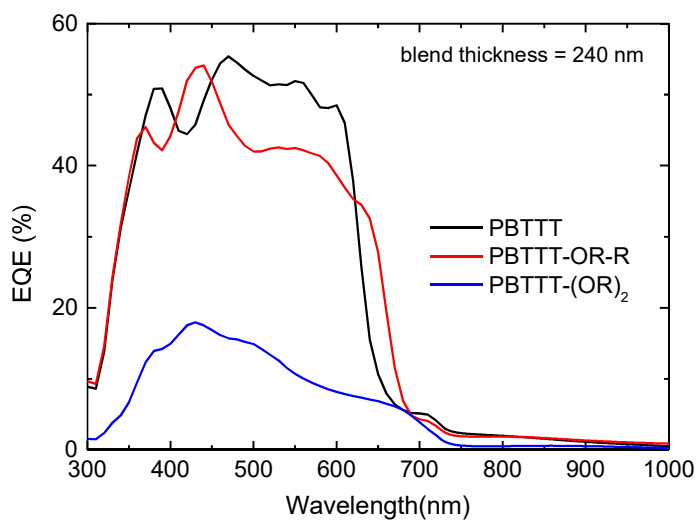
Figure S7: External quantum efficiencies for devices made from the polymer:$PC_{61}BM$ series (stack: glass/ITO/ZnO/active layer/MoO_3/Ag).
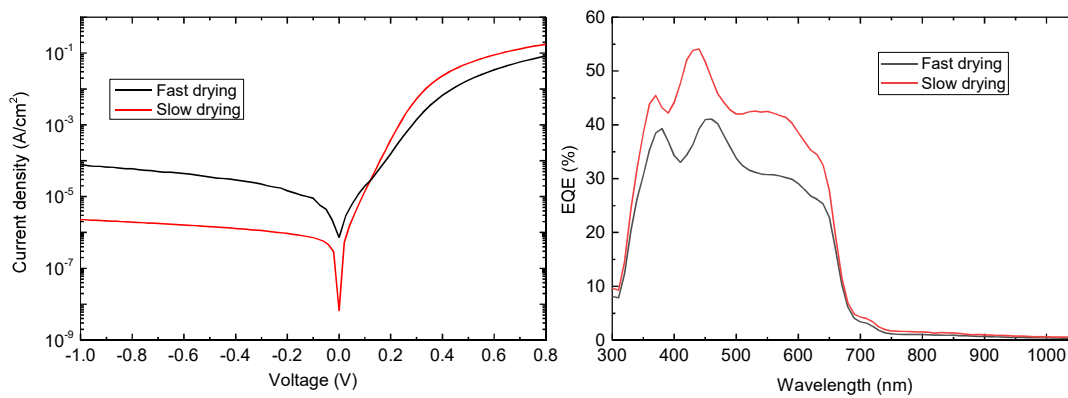
Figure S8: Influence of the drying process on the dark current (left) and the EQE (right) of a PBTTT-OR-R:$PC_{61}BM$ based device (fast drying: spin-coating for 60 s/60 °C for 5 min; slow drying: spin for 20 s (wet film) and dry in glovebox overnight; stack: glass/ITO/ZnO/PBTTT-OR-R:$PC_{61}BM$ (1:4)/MoO_3/Ag).
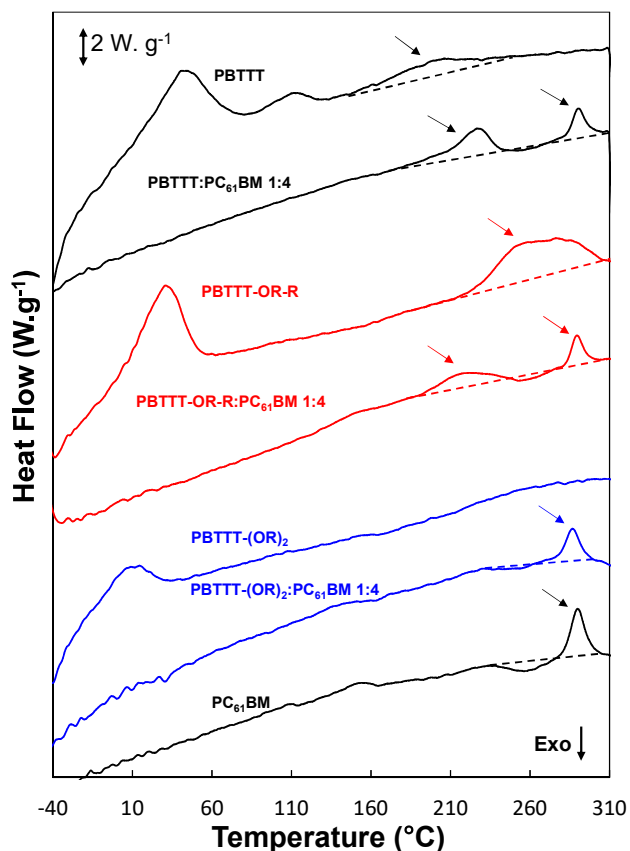
Figure S9: Rapid heat-cool calorimetry measurements (2nd heating) for the PBTTT polymer series, the respective 1:4 mixtures with $PC_{61}BM$, and pure $PC_{61}BM$. Arrows indicate the backbone melting of PBTTT and PBTTT-OR-R, the melting peak of $PC_{61}BM$, and the two new melting peaks observed for the 1:1 mixtures containing PBTTT and PBTTT-OR-R. The curves were vertically shifted for clarity.
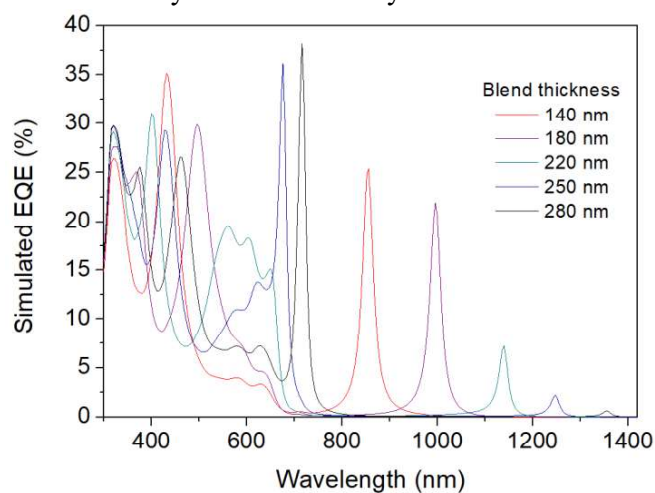

Figure S10: Simulation of the EQE of the cavity device with architecture glass (n=1.52)/Ag (25 nm)/ZnO-SG (25 nm)/ PBTTT-OR-R:$PC_{61}BM$ (140–280 nm)/MoO_3 (10nm)/Ag (100 nm). For the simulations, an IQE of 0.65 was assumed.
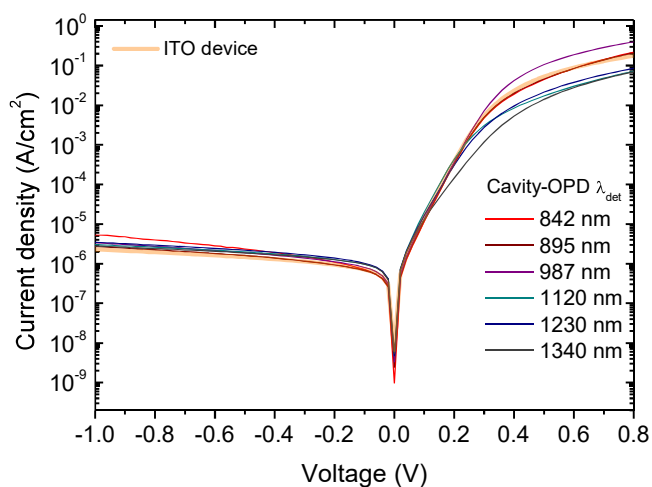
Figure S11: Dark current densities for the optimized cavity OPDs compared to the dark current of an ITO device (cavity stack: glass/Ag/ZnO/PBTTT-OR-R:$PC_{61}BM$ (1:4)/MoO_3/Ag; ITO stack: glass/ITO/ZnO/PBTTT-OR-R:$PC_{61}BM$ (1:4)/MoO_3/Ag).
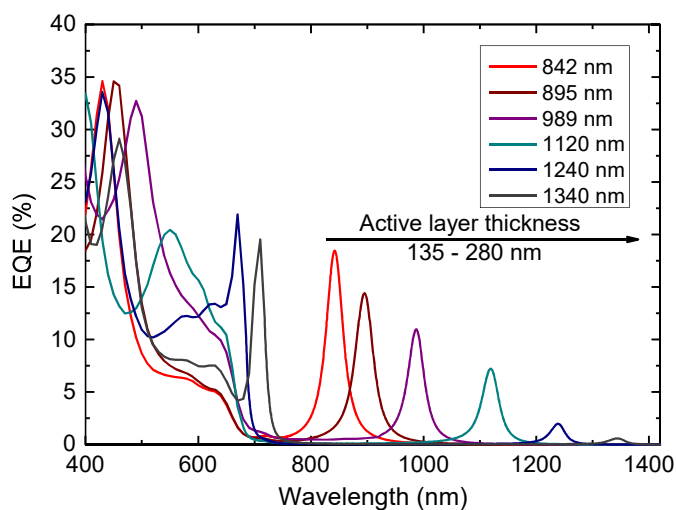
Figure S12: EQE spectra from 400 to 1400 nm for the metal-metal cavity devices with PBTTT-OR-R:$PC_{61}BM$ (1:4) active layer thicknesses ranging from 135 to 280 nm.
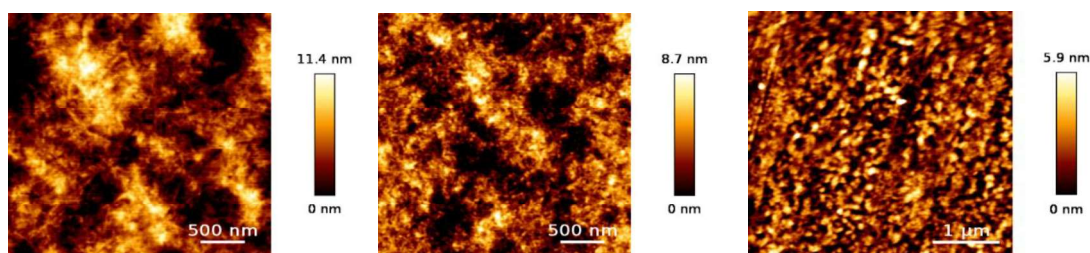
Figure S13: AFM images of PBTTT:$PC_{61}BM$ (left), PBTTT-OR-R:$PC_{61}BM$ (middle) and PBTTT-$(OR)_2$:$PC_{61}BM$ (right) active layer blends.

Table S3: Performance parameters of optical cavity-based NIR photodetectors.

Detector wavelength	EQE	R_{shunt}	j_{noise}	Spectral response	D^*	FWHM
[nm]	[%]	[$\Omega.cm^2$]	[$A.cm^{-1}.Hz^{-1/2}$]	[$A.W^{-1}$]	[Jones]	[nm]
842	18.3	1.1E+05	3.84E-13	1.24E-01	3.23E+11	35
895	14.2	1.4E+05	3.44E-13	1.02E-01	2.98E+11	38
987	10.8	1.2E+05	3.71E-13	8.60E-02	2.31E+11	35
1120	7.2	1.3E+05	3.62E-13	6.50E-02	1.80E+11	35
1236	2	1.3E+05	3.58E-13	1.99E-02	5.56E+10	30
1340	0.58	1.3E+05	3.58E-13	6.27E-03	1.75E+10	32

Figure S14: Light currents for the OPD devices based on PBTTT, PBTTT-OR-R and PBTTT-(OR)2 blended with $PC_{61}BM$ using the device stack glass/ITO/ZnO/active layer/MoO_3/Ag.

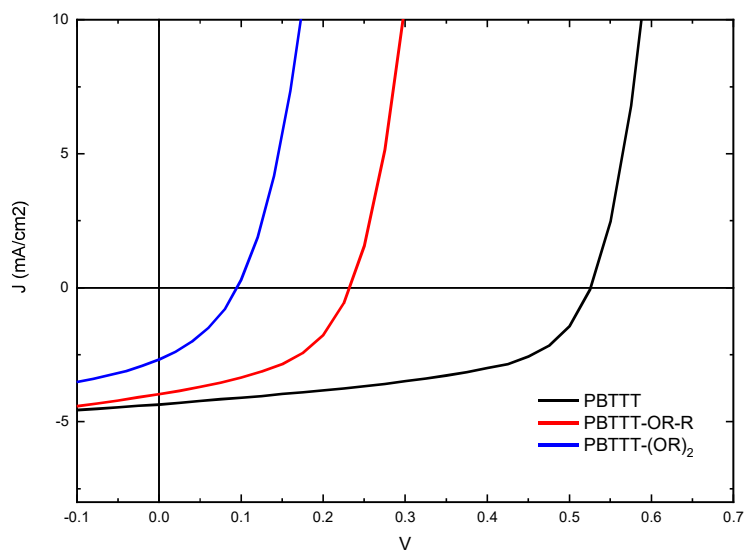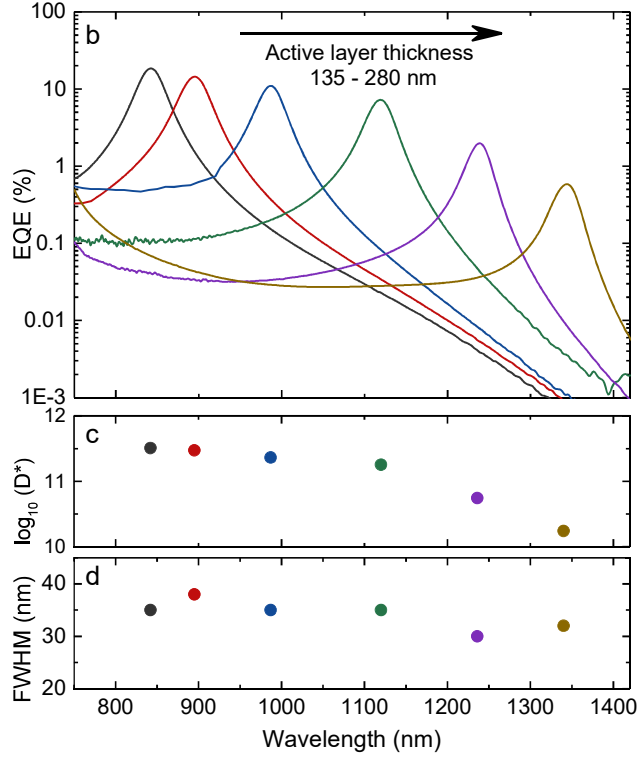**Figure S15:** (a) EQEs on a logarithmic scale for the metal-metal cavity devices with PBTTT-OR-R:PC$_{61}$BM (1:4) active layer thicknesses ranging from 135 to 280 nm. (b) Obtained detectivities between 842 and 1340 nm. (c) FWHM values of the resonance peaks.

Table S4: Literature overview of narrow-band and broad-band organic photodetector performance parameters.

	Narrow-band		
Ref	Wavelength [nm]	EQE [%]	*D** [Jones]
[5]	800	63	3.40E+12
[5]	800	68.5	5.90E+12
[6]	800	200	3.00E+11
[7]	810	0.5	
[8]	810	24.7	3.50E+12
[8]	835	29.6	5.70E+12
[9]	850	23	1.00E+12
[8]	860	21.2	4.20E+12
[10]	860	60	1.20E+13

S24

[11]	875	23	4.11E+11
[12]	890	2.8	1.29E+11
[12]	890	17.8	1.35E+12
[8]	907	25.9	8.60E+12
[7]	908	0.4	
[11]	910	21	3.90E+11
[11]	910		
[8]	910	22.4	4.70E+12
[10]	910	--	7.50E+12
[11]	935		
[10]	940	--	1.60E+13
[13]	946	8	4.60E+12
[11]	950	18	3.49E+11
[11]	960		
[8]	960	18.8	8.10E+12
[14]	980	3.2	1.70E+08
[12]	990	2.3	8.51E+10
[11]	995	7	1.42E+11
[8]	1000	2	1.10E+10
[7]	1032	0.4	
[11]	1035	5	1.06E+11
[8]	1060	0.9	9.00E+09
[11]	1085	1	2.21E+10
[11]	1100		
[7]	1150	0.2	4.00E+10
[12]	1200	0.08	6.42E+08

[8]	1200	0.7	7.00E+09
[12]	1210	0.23	1.79E+09
[7]	1244	0.15	
[8]	1255	0.7	7.00E+09
[7]	1370	0.1	
[12]	1390	0.06	4.69E+08
[8]	1425	0.09	1.00E+09
[7]	1484	0.05	
[8]	1580	0.02	8.00E+08
[7]	1581	0.02	
[8]	1645	0.01	1.00E+08
[7]	1665	0.005	3.00E+08
[15]	660	22.3	2.22E+11
[15]	710	18.4	1.97E+11
[15]	740	12.3	1.37E+11
[15]	810	12.9	1.58E+11
[15]	850	7.3	9.4E+10
[15]	920	9.7	1.35E+11
[15]	1000	7.5	1.13E+11
[15]	1080	7.1	1.16E+11
[15]	1130	6.5	1.11E+11
[15]	1190	6.8	1.22E+11
[15]	1250	4.2	7.8E+10
[15]	1295	3.5	6.9E+10
[15]	1360	1.9	3.9E+10
[15]	1390	1.4	3E+10

[15]	1450	0.6	1.2E+10
[15]	1505	0.3	6E+9
[15]	1170	2.5	3.43E+10
[15]	1220	2.9	4.03E+10
[15]	1250	2.7	3.95E+10
[15]	1290	2.9	4.17E+10
[15]	1340	2	3.08E+10
[15]	1330	2.5	3.79E+10
[15]	1400	1	1.66E+10
[15]	1510	0.2	2.84E+9
This work	**842**	**18.3**	**3.23E+11**
This work	**895**	**14.2**	**2.98E+11**
This work	**987**	**10.8**	**2.31E+11**
This work	**1120**	**7.2**	**1.80E+11**
This work	**1236**	**2**	**5.56E+10**
This work	**1340**	**0.58**	**1.75E+10**

Broad-band		
Ref	Wavelength (nm)	Detectivity (Jones)
[16]	1100	1.5E+12
[17]	1350	2.3E+10
[18]	900	1E+13
[18]	1200	5E+10
[18]	1200	8E+10
[19]	1500	1E+9
[20]	1600	1E+10

[21]	1100	3E+11
[22]	1300	1E+10
[23]	1050	2E+12
[24]	1050	1E+12
[25]	1000	1E+12
[26]	900	4E+13
[27]	1400	5E+9

3. References

[1]   M. J. Frisch, H. B. Schlegel, G. E. Scuseria, M. A. Robb, J. R. Cheeseman, G. Scalmani, V. Barone, B. Mennucci, G. A. Petersson, H. Nakatsuji, M. Caricato, X. Li, H. P. Hratchian, A. F. Izmaylov, J. Bloino, G. Zheng, J. L. Sonnenberg, M. Hada, M. Ehara, K. Toyota, R. Fukuda, J. Hasegawa, M. Ishida, T. Nakajima, Y. Honda, O. Kitao, H. Nakai, T. Vreven, J. A. Montgomery, Jr., J. E. Peralta, F. Ogliaro, M. Bearpark, J. J. Heyd, E. Brothers, K. N. Kudin, V. N. Staroverov, T. Keith, R. Kobayashi, J. Normand, K. Raghavachari, A. Rendell, J. C. Burant, S. S. Iyengar, J. Tomasi, M. Cossi, N. Rega, J. M. Millam, M. Klene, J. E. Knox, J. B. Cross, V. Bakken, C. Adamo, J. Jaramillo, R. Gomperts, R. E. Stratmann, O. Yazyev, A. J. Austin, R. Cammi, C. Pomelli, J. W. Ochterski, R. L. Martin, K. Morokuma, V. G. Zakrzewski, G. A. Voth, P. Salvador, J. J. Dannenberg, S. Dapprich, A. D. Daniels, O. Farkas, J. B. Foresman, J. V. Ortiz, J. Cioslowski, and D. J. Fox, Gaussian, Inc., Wallingford CT, **2016**.

[2]   Y. Zhao, D. G. Truhlar, *Theor. Chem. Acc.* **2008**, *120*, 215.

[3]   I. McCulloch, M. Heeney, C. Bailey, K. Genevicius, I. MacDonald, M. Shkunov, D. Sparrowe, S. Tierney, R. Wagner, W. Zhang, M. L. Chabinyc, R. J. Kline, M. D. McGehee, M. F. Toney, *Nat. Mater.* **2006**, *5*, 328.

[4]   K. Vandewal, K. Tvingstedt, A. Gadisa, O. Inganäs, J. V. Manca, *Phys. Rev. B* **2010**, *81*, 125204.

[5]   D. Leem, K. Lee, N. Li, B. W. Park, T. Choi, T. Ro, O. K. Kwon, Y. Kwon, T. N. Ng, S. Kim, *Adv. Opt. Mater.* **2021**, *9*, 2001682.

[6]   J. Miao, F. Zhang, M. Du, W. Wang, Y. Fang, *Adv. Opt. Mater.* **2018**, *6*, 1800001.

[7]   C. Kaiser, K. S. Schellhammer, J. Benduhn, B. Siegmund, M. Tropiano, J. Kublitski, D. Spoltore, M. Panhans, O. Zeika, F. Ortmann, P. Meredith, A. Armin, K. Vandewal, *Chem. Mater.* **2019**, *31*, 9325.

[8]   Z. Tang, Z. Ma, A. Sánchez-Díaz, S. Ullbrich, Y. Liu, B. Siegmund, A. Mischok, K. Leo, M. Campoy-Quiles, W. Li, K. Vandewal, *Adv. Mater.* **2017**, *29*, 1702184.

[9]   H. Zhang, S. Jenatsch, J. De Jonghe, F. Nüesch, R. Steim, A. C. Véron, R. Hany, *Sci. Rep.* **2015**, *5*, 9439.

[10]   B. Xie, R. Xie, K. Zhang, Q. Yin, Z. Hu, G. Yu, F. Huang, Y. Cao, *Nat. Commun.* **2020**, *11*, 2871.

[11]   B. Siegmund, A. Mischok, J. Benduhn, O. Zeika, S. Ullbrich, F. Nehm, M. Böhm, D. Spoltore, H. Fröb, C. Körner, K. Leo, K. Vandewal, *Nat. Commun.* **2017**, *8*, 15421.

[12]   Y. Wang, B. Siegmund, Z. Tang, Z. Ma, J. Kublitski, S. Xing, V. C. Nikolis, S. Ullbrich, Y. Li, J. Benduhn, D. Spoltore, K. Vandewal, K. Leo, *Adv. Opt. Mater.* **2021**, *9*, 2001784.

[13]   A. Armin, R. D. Jansen-van Vuuren, N. Kopidakis, P. L. Burn, P. Meredith, *Nat. Commun.* **2015**, *6*, 6343.

[14] S. B. Anantharaman, K. Strassel, M. Diethelm, A. Gubicza, E. Hack, R. Hany, F. A. Nüesch, J. Heier, *J. Mater. Chem. C* **2019**, *7*, 14639.

[15] J. Yang, J. Huang, R. Li, H. Li, B. Sun, Q. Lin, M. Wang, Z. Ma, K. Vandewal, Z. Tang, *Chem. Mater.* **2021**, DOI: 10.1021/acs.chemmater.1c01196.

[16] X. Gong, M.-H. Tong, S. H. Park, M. Liu, A. Jen, A. J. Heeger, *Sensors* **2010**, *10*, 6488.

[17] J. D. Zimmerman, V. V. Diev, K. Hanson, R. R. Lunt, E. K. Yu, M. E. Thompson, S. R. Forrest, *Adv. Mater.* **2010**, *22*, 2780.

[18] J. Qi, J. Han, X. Zhou, D. Yang, J. Zhang, W. Qiao, D. Ma, Z. Y. Wang, *Macromolecules* **2015**, *48*, 3941.

[19] M. Young, J. Suddard-Bangsund, T. J. Patrick, N. Pajares, C. J. Traverse, M. C. Barr, S. Y. Lunt, R. R. Lunt, *Adv. Opt. Mater.* **2016**, *4*, 1028.

[20] J. Han, J. Qi, X. Zheng, Y. Wang, L. Hu, C. Guo, Y. Wang, Y. Li, D. Ma, W. Qiao, Z. Y. Wang, *J. Mater. Chem. C* **2017**, *5*, 159.

[21] M.-S. Choi, S. Chae, H. J. Kim, J.-J. Kim, *ACS Appl. Mater. Interfaces* **2018**, *10*, 25614.

[22] Z. Wu, W. Yao, A. E. London, J. D. Azoulay, T. N. Ng, *Adv. Funct. Mater.* **2018**, *28*, 1800391.

[23] F. Yang, C. Li, Y. Wei, N. Yan, X. Wang, F. Liu, S. You, J. Wang, W. Ma, W. Li, *Macromol. Rapid Commun.* **2018**, *39*, 1800546.

[24] F. Verstraeten, S. Gielen, P. Verstappen, J. Kesters, E. Georgitzikis, J. Raymakers, D. Cheyns, P. Malinowski, M. Daenen, L. Lutsen, K. Vandewal, W. Maes, *J. Mater. Chem. C* **2018**, *6*, 11645.

[25] J. Huang, J. Lee, J. Vollbrecht, V. V. Brus, A. L. Dixon, D. X. Cao, Z. Zhu, Z. Du, H. Wang, K. Cho, G. C. Bazan, T. Nguyen, *Adv. Mater.* **2020**, *32*, 1906027.

[26] G. Liu, T. Li, X. Zhan, H. Wu, Y. Cao, *ACS Appl. Mater. Interfaces* **2020**, *12*, 17769.

[27] F. Verstraeten, S. Gielen, P. Verstappen, J. Raymakers, H. Penxten, L. Lutsen, K. Vandewal, W. Maes, *J. Mater. Chem. C* **2020**, *8*, 10098.